Geosystems and Geoenvironment 2 (2023) 100108

Contents lists available at ScienceDirect

Geosystems and Geoenvironment

journal homepage: www.elsevier.com/locate/geogeo

From an atomistic study of olivine under pressure to the understanding of the macroscopic energy release in earthquakes

Maurizio Mattesini[a,b,*], Carolina López Sánchez[a], Elisa Buforn[a,b], Agustín Udías[a], Jaime de la Serna Valdés[a], Hernando Tavera[c], Carmen Pro[d]

[a] Department of Earth's Physics and Astrophysics, Complutense University of Madrid, Madrid E-28040, Spain
[b] Facultad de Ciencias Físicas, Instituto de Geociencias (UCM-CSIC), Plaza de Ciencias 1, Madrid E-28040, Spain
[c] Instituto Geofísico del Perú, Calle Badajoz 169, Lima 15012, Perú
[d] Departamento de Física, Centro Universitario de Mérida, Universidad de Extremadura, Mérida, Badajoz E-06800, Spain

ARTICLE INFO

Article history:
Received 22 March 2022
Revised 13 June 2022
Accepted 21 July 2022

Editor: A. Vasanthi

Keywords:
Peruvian-Brazilian subduction zone
Atomistic rupture process
Elasticity and anelasticity
Intermediate and very deep earthquakes
Earthquake energy budget

ABSTRACT

We present a multi-disciplinary study of the rupture process of deep- and intermediate-depth earthquakes in the subducting slab that develops beneath the Peruvian-Brazilian region. This contemplates the understanding of the atomistic fracture mechanism in an olivine model, its energetics budget, and the bridging of these results to the available seismic observables. A theoretical description of the stress-strain curves for the subducting material is initially provided as a key element to discern whether the rupture mechanism changes with depth or not. To this purpose, atomistic modelling was carried out through *ab initio* techniques for the forsterite olivine at different pressure ranges. The achieved stress-strain curves were compared to the average moment-scaled functions obtained for 43 intermediate (50 km $< h <$ 200 km) and very deep earthquakes (500 km $< h <$ 700 km) at the Peruvian-Brazilian subduction zone. It is found that at both depths operate a common atomistic rupture mechanism that is based on the gliding of the {001} crystal planes. Although the velocity of stress release changes with depth, this finding helps to clarify the controversial rupture process for very deep earthquakes at subduction zones. Likewise, efforts were directed to quantify the total amount of energy freed during an earthquake. Test calculations were carried out for several deep earthquakes providing rupture energy of six orders of magnitudes larger than the observable radiated seismic energy. This indicates that there might be space for redefining the commonly accepted order of magnitude for the seismic efficiency coefficient.

1. Introduction

The occurrence of intermediate and deep earthquakes is generally explained in terms of the subduction process. The collision between a continental and an oceanic lithosphere plate makes the latter dive beneath the warmer and less dense continental plate and sink into the surrounding mantle. The dipping oceanic lithosphere drags the rest of the tectonic plate and this represents the main cause of the well-known plate motion mechanism. The plunging wedge of the oceanic lithosphere experiences a variety of deep and intermediate-depth earthquakes. The models used to investigate the rupture process in such events are generally referring to mechanical models that consider the earth as a homogeneous or inhomogeneous elastic media, where the atomistic characteristics of the material are not explicitly considered. Hence, both form and amount of energy released during an earthquake must be reviewed by exploring the possibility of a more complex microscopic mechanism. Also, it is well known that by increasing depth, both pressure and temperature conditions rise as to provide a viscoelastic media that will unlikely experiment a fragile rupture. This leads to a situation where the occurrence of deep and intermediate-depth earthquakes becomes difficult to explain. Besides, the amount of total energy released by an earthquake represents another long-standing unsolved question in seismology. From seismograms, it is only possible to estimate the radiated seismic energy, which is just a portion of the earthquake total energy. A not well constrained seismic efficiency coefficient (η) is often used to approximate the total earthquake energy (Spudich, 1992; Guatteri and Spudich, 1998; Kanamori et al., 1998; Kanamori and Rivera, 2006; Terakawa and Hauksson, 2018). Kikuchi (1992) reported $0.012 \leq \eta \leq 0.22$ for several large earthquakes and stated that deep events have a smaller value than shallow ones. From laboratory experiments and mining-

---

* Corresponding author at: Department of Earth's Physics and Astrophysics, Complutense University of Madrid, Madrid E-28040, Spain.
E-mail address: mmattesi@ucm.es (M. Mattesini).

https://doi.org/10.1016/j.geogeo.2022.100108

induced events, McGarr (1994) also specified the hypothesis that $\eta \leq 0.06$. However, due to the general difficulty in accessing the absolute stress, the binding of η to a well-defined range of values is hardly accessible through seismology. From this point of view, the consideration of an atomistic mechanism may help to shed light on the total energy generated by an earthquake and to bound the magnitude of the efficiency factor.

The faulting mechanism of deep earthquakes is still enigmatic and could differ from that of intermediate and shallow events. As such, the rising of pressure and temperature with depth tend to inhibit brittle failure and promote ductile flow. Several mechanisms have been proposed so far, including shear thermal instability (Ogawa, 1987; Kanamori et al., 1998), dehydration embrittlement (Meade and Jeanloz, 1991; Silver et al., 1995), and transformational faulting (Green and Burnley, 1989; Kirby et al., 1991; Green and Houston, 1995, 1996; Ohuchi et al., 2017). Intermediate-depth earthquakes (70 km < depth < 300 km) are generally attributed to dehydration embrittlement (Kirby et al., 1996; Peacock and Wang, 1999; Hacker et al., 2003; Ohuchi et al., 2018) or embrittlement due to dehydration-driven stress transfer (Ferrand et al., 2017), although thermal shear instability has also been suggested as plausible (Kelemen and Hirth, 2007; Prieto et al., 2013; Poli et al., 2016). For deep-focus earthquakes (depth > 300 km), phase transformational faulting and thermal instability have so far gained the most evidence (Wiens, 2001; Houston, 2007). It has also been suggested that deep earthquakes may have more than one mechanism, depending on the slab conditions (Frohlich, 2006; Houston, 2007; Wiens and McGuire, 1995; Wiens and Gilbert, 1996). However, novel mechanisms or hypotheses such as olivine-to-spinel phase transition in metastable olivine (Schubnel et al., 2013; Wang et al., 2017) continue to emerge in this active field of research. Also, Liu and Zhang (2015) proposed that internal stress induced by differential shortening of subducted crust and mantle is responsible for the depth distribution of deep earthquakes.

Deep earthquakes exhibit diverse characteristics, possibly more diverse than shallow/intermediate earthquakes. For example, *b*-values in Gutenberg-Richter distributions have large regional variations for deep-focus events, e.g., $b \approx 0.4$ for South America and $b \approx 1.2$ for Tonga (Houston, 2007; Frohlich, 1989; Frohlich and Davis, 1993). About 85% of the rupture velocities for deep earthquakes fall between $0.3V_S$ and $0.9V_S$ (where V_S is the shear wave speed), a greater range than it is seen for shallow earthquakes (Frohlich, 2006). Other parameters such as scaled source duration, stress drop, and radiation efficiency also show strong variability and possible dependences on event magnitudes, depths, and tectonic settings (Wiens, 2001; Frohlich, 1989; Houston and Williams, 1991; Vidale and Houston, 1993; Houston, 1993; Houston and Vidale, 1994; Houston et al., 1998; Houston, 2001; Poli and Prieto, 2014, 2016). This diversity, while often entangled with limited resolution, is critical in understanding the sensitivity of deep earthquake mechanisms to various physical conditions. For example, Wiens (2001) summarized the temperature dependence of deep-focus earthquake source parameters and argued in favour of thermally controlled mechanisms, such as shear thermal instability (Ogawa, 1987).

In consequence, understanding the rupture mechanism of earthquakes inside a subducting slab requires a thorough knowledge of the mineral physics of the sinking material as well as that of the surrounding media. We hereby assume that the mineral olivine (Fig. 1) is the primary component of the Earth's upper mantle and thus of the subducting lithosphere. This mineral is a magnesium iron silicate with formula $(Mg^{2+}, Fe^{2+})_2SiO_4$, where the ratio of magnesium to iron varies between the two end-members of the solid solution series: The Mg-end-member forsterite (Mg_2SiO_4) and the Fe-end-member fayalite (Fe_2SiO_4). As depth increases, the abundant mineral olivine undergoes several phase changes (Moore and Smith, 1969; Baur, 1972). Transitions in $(Mg, Fe)_2SiO_4$, from the α (olivine) phase to the β (wadsleyite) phase and from β to γ (ringwoodite), are believed to occur near 410 km and 520 km, respectively, under normal mantle conditions, accounting for the well-known seismic discontinuities at those depths (Katsura and Ito, 1989; Bina, 1991). Inside the relatively cold subducting slab, however, the phase change from olivine to wadsleyite may be delayed, allowing the α-$(Mg, Fe)_2SiO_4$ to persist metastably into a high-pressure stability field (Sung and Burns, 1976). Previous studies indicate that metastable $(Mg_{1.8}Fe_{0.2})SiO_4$ olivine could survive to depths greater than 500 km in the cold interior of rapidly subducting slabs of the old lithosphere (Rubie and Ross, 1994). Interesting seismic evidence for such a Metastable Olivine Wedge (MOW) in subducting zones like the Pacific slab under the Japan Sea was also provided (Jiang et al., 2008; Kawakatsu and Yoshioka 2011; Shen and Zhan, 2020). The MOW might act as a low-density material, reducing the descent velocity of the slab (Kirby et al., 1996). Lower plunging rates would allow slabs to warm and metastable wedges to thermally erode (Marton et al., 1999). The persistence of metastable olivine (i.e., a sort of cold olivine) to depths greater than 400 km in subducting slabs has strong implications for the generation of deep-focus earthquakes.

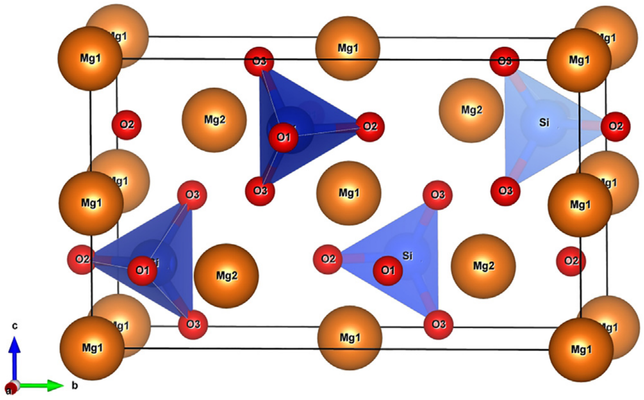

Fig. 1. Periodic crystal structure of olivine (*Pbnm* space group setting). While silicon atoms are tetrahedrally coordinated by four oxygens (blue polyhedral), magnesium atoms are octahedrally coordinated by six oxygens (for clarity, these polyhedral are not shown in the figure). This figure was generated by using the VESTA visualization software program (Momma and Izumi, 2011).

In this work, we study the atomistic mechanism of intermediate and deep earthquakes in the Peruvian-Brazilian region (Figs. 2 and 3), which is a subduction zone associated with the contact between the Nazca and the South America Plates. The subduction extends from 8°S to 20°S along with Peru and shows a convolute rupture characteristic. It starts at the Peru-Chile Trench located offshore near the west of Peru (Fig. 2) with a convergence rate of about 7.0–8.5 cm/yr along an azimuth of 80°N (Minster and Jordan, 1978; DeMets et al., 2010; Somoza and Ghidella, 2012; Stein et al., 1986; DeMets et al., 1990, 1994; Argus and Heflin, 1995; Norabuena et al., 1998; Angermann et al., 1999, 1999; Kendrick et al., 2003). The two main characteristics of this subduction area are the alternative regions of normal and flat subduction and the absence of earthquakes in the depth range from 300 to 500 km. From 3°S to 15°S the Nazca plate subducts at an angle of 30° until reaches 100 km depth where it flattens down for several hundred km. On the other hand, starting from 15°S the plate subducts with a continuous dip angle of 30° (Cahill and Isacks, 1992; Hayes et al., 2012; Phillips et al., 2012; Phillips and Clayton, 2014; Kim and Clayton, 2015; Ma and Clayton, 2015; Bishop et al., 2017; Lim et al., 2018;

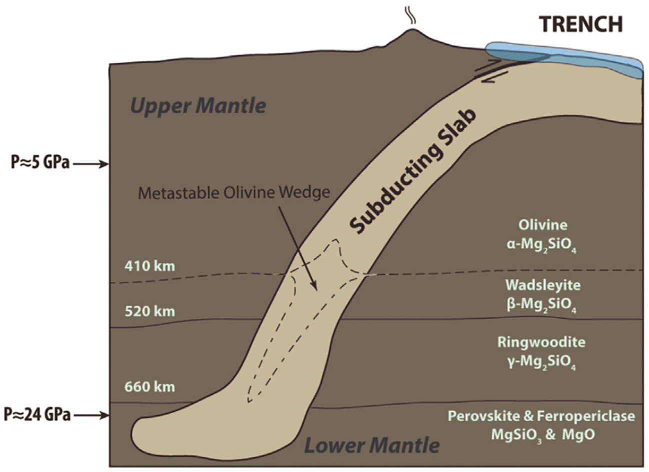

Fig. 2. Subducting slab made of stable (shallower than ∼400 km depth) and metastable (deeper than ∼400 km depth) olivine mineral.

Gutscher et al., 2000; Tavera and Buforn, 2001). The age of the developing flat slab was estimated to be 11.2 Myr (Chlieh et al., 2011; Lim et al., 2018). The observed seismicity in this region is a consequence of these plate boundaries. From Fig. 4 we observe that for the period 1990–2020, shallow earthquakes ($h < 60$ km) are mainly located between the trench and the coast with some events inside the continental plate. A typical feature of this shallow seismicity is the frequent occurrence of earthquakes with large magnitudes (Mw > 7) along the coastline. During the last two decades, six such events have so far occurred (2018, 2014, 2013, 2007, and two in 2001). The most active zone corresponds to southern Peru and northern Chile between 13°S and 20°S, while seismicity generally decreases when moving up north. Intermediate depth seismicity (60 km $< h <$ 350 km) is observed parallel to the coast and between the Cordillera Occidental and the SubAndean zone, with maximum activity in the southern Altiplano. The intermediate-depth earthquakes are distributed from 0°S to 6°S between the coast and the interior of the continent where a maximum depth of 200 km is reached. In the central region, between 6°S and 13°S, a narrow gap of epicenters appears parallel to the coastline that may be correlated to the flat subduction in this zone.

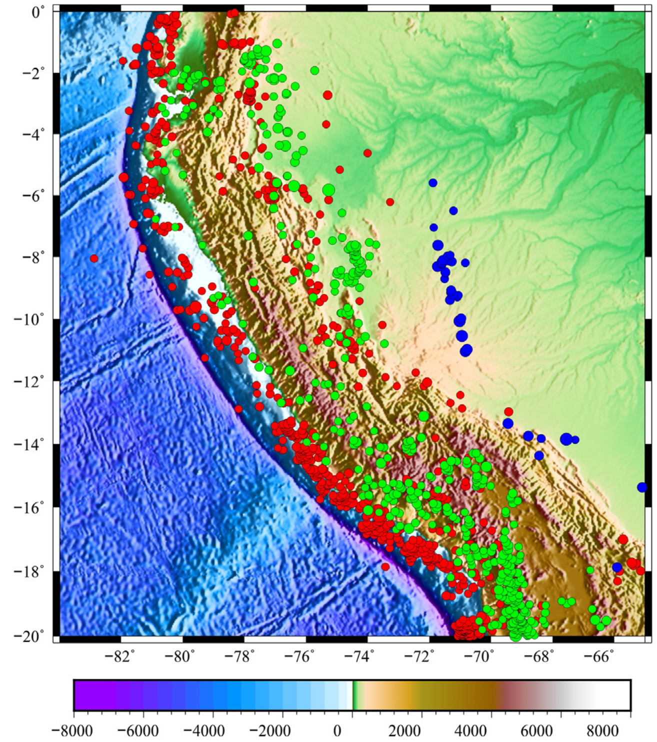

Fig. 4. Distribution of epicenters for the period 1990–2020 (magnitudes ≥ 5) taken from USGS catalogue, https://earthquake.usgs.gov/earthquakes/search/). Green circles correspond to shallow earthquakes ($h \le 60$ km), red to intermediate depth (60 $< h \le$ 350 km) and blue to deep ($h >$ 350 km). The bathymetry of this figure is taken from https://www.gmrt.org/.

From 13°S to 20°S, where the slab subducts with a dipping angle of 30°, the intermediate-depth seismicity is more active, reaching depths larger than 200 km. The very deep earthquakes (500 km $< h <$ 700 km) are mostly localized within the central region of the Peru-Brazil border and Bolivia, somewhere in between 6°S and 14°S.

The main goal of this work is to study the rupture process of deep and intermediate-depth earthquakes along with subducting slabs. This means understanding the theoretical fracture mecha-

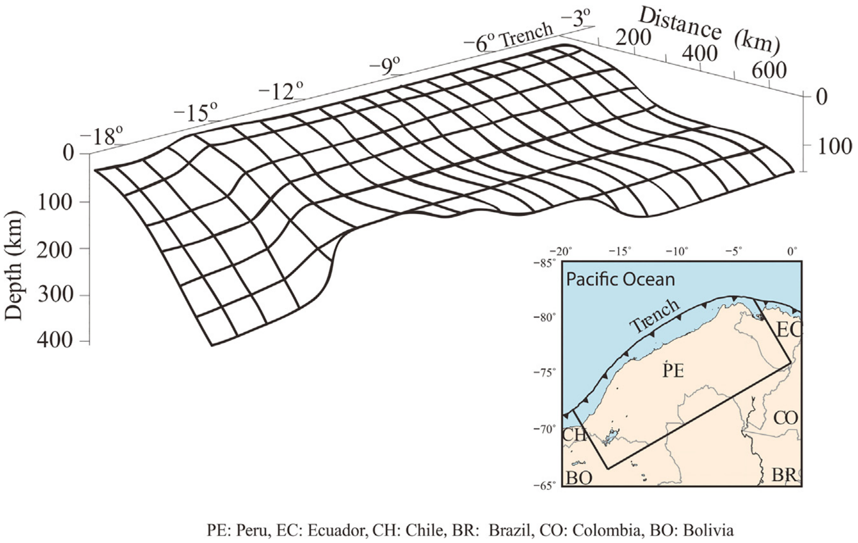

Fig. 3. The subduction scheme of the Nazca plate under the South America. PE = Perú, EC = Ecuador, CH = Chile, BO = Bolivia, BR = Brazil, CO = Colombia (modified from Tavera and Buforn 2001).

nism and the energetics balance in a forsterite olivine model (or a MOW model for depths greater than 400 km) with the final aim to bridge these results to the available seismic observables. Towards this ultimate goal of resolving the nature of the focal mechanism in both intermediate and deep earthquakes, we present a multidisciplinary work where observable seismic features are bridged to the outcome of quantum-mechanical atomistic calculations. The latter methodology provides important microscopic material properties that are of fundamental interest in identifying key macroscopic fracture features that are directly coupled to seismic observables. As an example, we examine the validity of the faulting mechanism and the robustness of the cold olivine hypothesis. This is accomplished by studying the dependence of the focal mechanism with depth at the Peruvian-Brazilian subduction zone and applying the *first-principles* stress-strain relationships of the atomistic model to the observed moment rate functions of 43 intermediate and deep earthquakes of this region.

2. Materials and methods

In this section, we provide the fine-scale physics and structure (i.e., the behaviour of electrons, ions, and their assemblies) of MOW under shear-stress conditions. It is understood that a complementary description of the same material at a coarse-scale would also be highly desirable. However, it is generally known that mesoscopic and multiscale modelling relies strongly on available experimental data rather than the theory used for the calculational scheme (Fish et al., 2021). The lack of such data for olivine at very deep mantle conditions makes it appropriate to focus first our efforts on the *ab initio* scale and save the upscale to a coarser system for possible future works. Likewise, considering that grain size in experimental olivine samples can be of the order of µm (Ferreira et al., 2021) and that its unit-cell has an average density of $\approx 10^{23}$ atoms/cm^3, achieving trustable results for aggregates (i.e., with an accuracy similar to *ab initio* methods) becomes prohibitive even with classical molecular dynamics techniques. The size of the supercell that one must handle to describe a few grains would easily reach the technical limitations imposed by the actual computer power ($\approx 10^{12}$ atoms for a simple Lennard-Jones potential in exascale computers). Therefore, it is worth remarking that due to the enormous computational complexity involved, multiscale modelling of inter- and intra-granular mechanisms in a polycrystalline olivine aggregate remains nowadays a very challenging task.

2.1. Atomistic structure calculations

A thorough atomistic study of the elasto-plastic deformations on homogeneous solid olivine can help to better understand the controversial source mechanism that is at the origin of the very deep earthquakes. In the following, we start by providing the essential technical details of the chosen atomistic computational scheme for assessing the physical properties of olivine.

The atomic structure of forsterite olivine (α-Mg_2SiO_4) was studied with the VASP code (Kresse and Furthmüller, 1996; Kresse and Joubert, 1999) that solves the Scrhödinger-like Kohn-Sham equations according to the formalism the *Density Functional Theory* (DFT; Hohenberg and Kohn, 1964; Kohn and Sham, 1965). The interaction between the ions and the electrons was described by using potentials generated with Blöchl's Projector Augmented Wave (PAW) method (Blöchl, 1994). The PAW potentials used to treat the valence configuration of Mg, O, and Si were $3s^2$, $2s^2$ $2p^4$, and $3s^2$ $3p^2$, respectively. The electron-electron interaction was described by using the parametrization of Perdew et al. (1996) for the exchange-correlation functional. *First-principles* calculations were completed with an energy cut-off of 600 eV for the plane-wave basis set and converged with respect to the **k**-point integration. Brillouin zone integrals were approximated by using the special **k**-point sampling of Monkhorst and Pack (1976) with a 13 × 9 × 11 grid. Finally, it is worth mentioning that before performing any specific calculation on the strained α-Mg_2SiO_4 model, the structural parameters of the unit cell were first optimized at the desired target pressure. This allowed setting the unstrained system at its ground state energy. In Table 1, we list the computed equilibrium parameters for two different pressure/depth values with an energy convergence of 0.01 eV/Å. The achieved structural parameters and densities agree rather well with the experimental data of Zha et al. (1998) for the natural samples of San Carlos olivine $[(Mg_{0.9}Fe_{0.1})_2SiO_4]$ and with earlier theoretical studies of forsterite (Brodholt et al., 1996).

2.1.1. Elastic behaviour

In what follows we explain how the complete set of elastic constants (C_{ij}) can be computed for a given crystalline material. The elastic constants determine the response of the crystal to an externally applied strain and provide information about the bonding characteristics between adjacent atomic planes, the anisotropic character of the bonding, and structural stability. The main problem in estimating elastic constants from *first principles* is not only the requirement of accurate methods for evaluating the total energy but also the heavy computations involved in their calculation. For low-symmetry systems, the number of independent moduli increases, and a larger number of distortions is required to calculate the full set of C_{ij}. The elastic behaviour of a completely asymmetric material is specified by 21 independent elastic constants, while for an isotropic material this number reduces to two. In between these limits, the necessary number is determined by the crystal symmetry (Nye, 1985). For an orthorhombic material like olivine, there exist nine independent elastic constants referred to as C_{11}, C_{22}, C_{33}, C_{44}, C_{55}, C_{66}, C_{12}, C_{13}, and C_{23}. They can be deduced by applying small strains to the equilibrium lattice and determining the resulting change in the total energy (Mattesini and Matar, 2002). In this study, the athermal elastic constants of olivine were computed by employing the computational tool of *MedeA* (a trademark of Materials Design), which uses a symmetry-general formulation of the elastic constants from total energy calculations (Le Page and Saxe, 2001, 2002). The stress tensor, i.e., the derivatives of the total energy of the cell with respect to changes of the lattice parameters (cell lengths and angles), was computed with the VASP code by means of specific analytic expressions. The achieved C_{ij} at two different pressure/depth values are shown in Table 2 together with their polycrystalline averaged (Hill, 1952), bulk (B), shear (G), Young (E) moduli, and the compressional (V_P) and shear (V_S) velocities. Errors with respect to experimental data (Zha et al., 1998) in the longitudinal moduli (C_{11}, C_{22}, C_{33}) are within 1.2–7.0%, in the shear moduli (C_{44}, C_{55}, C_{66}) 0.9–8.4%, and in the off-diagonal moduli (C_{12}, C_{13}, C_{23}) 2.4–9.8%. The aggregate bulk and shear moduli calculated from the single-crystal stiffnesses are also in good agreement with the experimental data of Zha et al. (1998).

The analysis of the lattice stability for crystals under constant hydrostatic pressure was originally proposed by Milstein and Hill (1979) who showed that the combined incremental potential energy of the crystal and its external loading must be positive for small lattice deformations. The requirement for mechanical stability in an orthorhombic crystal under a hydrostatic pressure P leads to the following restrictions on the elastic constants (Sin'ko et al., 2002; Chen et al., 2019):

$$\begin{aligned}&\widetilde{C_{11}}+\widetilde{C_{22}}-2\widetilde{C_{12}}>0,\ \widetilde{C_{11}}+\widetilde{C_{33}}-2\widetilde{C_{13}}>0,\ \widetilde{C_{22}}+\widetilde{C_{33}}-2\widetilde{C_{23}}>0\\&\widetilde{C_{ii}}>0\ (\forall\ i=1,\ 2,\cdots,\ 6),\widetilde{C_{11}}+\widetilde{C_{22}}\ +\widetilde{C_{33}}+2\widetilde{C_{12}}+2\widetilde{C_{13}}\\&\quad+2\widetilde{C_{23}}>0\end{aligned} \qquad (1)$$

Table 1
Optimized olivine PBE-GGA structural parameters at $P \neq 0$ and $T = 0$ K. For comparison, values within round parenthesis refer to the experimental data of Zha et al. (1998) for the natural San Carlos olivine at both 5 and 24 GPa.

Property	$P = 5$ GPa / depth=155 km	$P = 24$ GPa / depth=670 km
Crystal system	Orthorhombic	Orthorhombic
Space group	*Pbnm* (#62)	*Pnnm* (#62)
Atom type (Wyckoff site)	x/*a* y/*b* z/*c*	x/*a* y/*b* z/*c*
Mg_1 (4a)	0.0000 0.0000 0.0000	0.0000 0.0000 0.0000
Mg_2 (4*c*)	0.9906 0.2765 0.2500	0.9885 0.2747 0.2500
Si (4*c*)	0.4263 0.0943 0.2500	0.4263 0.0955 0.2500
O_1 (4*c*)	0.7678 0.0918 0.2500	0.7702 0.0912 0.2500
O_2 (4*c*)	0.2227 0.4452 0.2500	0.2248 0.4413 0.2500
O_3 (8*d*)	0.2746 0.1641 0.0309	0.2685 0.1671 0.0262
Cell constants and density		
a (Å)	4.7529 (4.724)	4.6404 (4.613)
b (Å)	10.1279 (10.065)	9.6648 (9.593)
c (Å)	5.9540 (5.925)	5.7314 (5.708)
a, b, g (°)	90, 90, 90	90, 90, 90
r (g/cm^3)	3.261 (3.466)	3.636 (3.865)

Table 2
Theoretical single-crystal elastic constants and averaged quantities for the cold olivine model phase at different pressures/depths. For comparison, experimental data of Zha et al. (1998) for the natural San Carlos olivine are shown at both 5 and 24 GPa.

Elastic constant	$P = 5$ GPa / depth=155 km	$P = 24$ GPa / depth=670 km
C_{11} (GPa)	340.89 ± 8.75 (352.8 ± 11.4)	458.95 ± 9.42 (442.2 ± 12.0)
C_{12}	82.23 ± 6.19 (91.2 ± 7.6)	150.40 ± 6.66 (138.8 ± 13.0)
C_{13}	83.79 ± 6.19 (92.7 ± 7.4)	152.24 ± 6.66 (148.7 ± 8.2)
C_{22}	215.34 ± 8.75 (224.2 ± 7.2)	302.22 ± 9.42 (292.0 ± 13.2)
C_{23}	86.39 ± 6.19 (95.2 ± 5.2)	152.13 ± 6.66 (161.7 ± 8.2)
C_{33}	247.75 ± 8.75 (267.1 ± 8.2)	335.87 ± 9.42 (339.8 ± 10.0)
C_{44}	70.18 ± 12.38 (70.8 ± 1.6)	94.35 ± 13.32 (87.6 ± 2.1)
C_{55}	82.52 ± 12.38 (85.7 ± 2.3)	98.99 ± 13.32 (102.5 ± 1.7)
C_{66}	84.13 ± 12.38 (90.2 ± 2.2)	108.41 ± 12.32 (118.4 ± 3.1)
B	143.26 (153.5)	219.93 (216.8)
G	82.81 (85.5)	101.76 (101.2)
E	208.29	264.48
θ_D (K)	773.1	856.3
V_P (km/s)	9.00 (8.79)	10.47 (9.54)
V_S (km/s)	5.14 (4.97)	5.60 (5.12)

where $\widetilde{C_{ii}} = C_{ii} - P$ $(\forall\ i = 1,\ 2, \cdots,\ 6)$, $\widetilde{C_{12}} = C_{12} + P$, $\widetilde{C_{13}} = C_{13} + P$, $\widetilde{C_{23}} = C_{23} + P$. It is worth noting that the two sets of C_{ij} shown in Table 2 satisfy all the above conditions, indicating that the cold olivine system is mechanically stable at the investigated pressures/depths. Therefore, even though olivine is not the most energetically favoured Mg_2SiO_4 structure at these depths, it is at least a metastable solid-state system. The results shown in Table 2 indicate a general strengthening of the elastic constants with increasing depth. The same tendency is also observed for the polycrystalline Young, shear, and bulk moduli, as well as for the compressional and shear velocities. This mechanical trend is in line with the increasing density of olivine with increasing depth (cf. the equilibrium density values (ρ) in Table 1). For instance, a measure of the stiffness of the solid is given by Young's modulus, which defines the ratio between linear stress and strain. As a rule of thumb, the larger the value of *E*, the stiffer is the material. We found that this magnitude increases with depth just as in the case of *B* and *G*.

By computing the *B/G* ratio, we can further estimate the brittle and ductile behaviour of the polycrystalline olivine system by considering the shear modulus as the resistance to plastic deformation and the bulk modulus as the resistance to fracture. Within this basic approach, a high (low) *B/G* ratio becomes associated with the ductility (brittleness) of the investigated material. The critical number that separates the ductile and the brittle behaviour was fixed at about 1.75 by Pugh (1954). Higher *B/G* ratios are then associated with ductility and lower ones to brittleness. Accordingly, the cold olivine behaves as a brittle model phase ($B/G = 1.73$) at low pressures (e.g., $P = 5$ GPa), while tends to be more ductile ($B/G = 2.16$) at larger pressure values (e.g., $P = 24$ GPa). Therefore, within the elastic limit scenario, the single-crystal cold olivine becomes harder and stiffer with increasing depth, while its ductility, as a polycrystalline material, seems to increase.

Another fundamental parameter that correlates with many physical properties of solids, such as specific heat, elastic constants, and melting temperature is the Debye temperature (θ_D). By making use of the simple Debye-Grüneisen model (Anderson, 1963), the magnitude of θ_D can be defined in terms of the mean sound velocity (V_m) to provide explicit information about lattice vibrations (Ibrahim, 1988):

$$V_m = \left[\frac{1}{3}\left(\frac{2}{V_S^3} + \frac{1}{V_P^3}\right)\right]^{-1/3} \tag{2}$$

Accordingly, the Debye temperature can be obtained by the following equation:

$$\theta_D = \frac{h}{k}\left[\left(\frac{3n}{4\pi}\left(\frac{N_A \rho}{M}\right)\right)\right]^{1/3} V_m, \tag{3}$$

where *h* is the Plank's constant, *k* the Boltzmann's constant, N_A the Avogadro's number, ρ the density, *M* the molecular weight, and *n* the number of atoms within the unit-cell. As a general criterion, the higher the θ_D, the greater the thermal conductivity. The calculation of θ_D for olivine at two different target depths (Table 2) indicates a clear increase of θ_D with increasing pressure/depth.

Table 3
Theoretical anisotropy factor for the cold olivine model at different pressures/depths. Experimental values of Zha et al. (1998) are shown inside round parenthesis.

Anisotropy factor	$P = 5$ GPa / depth=155 km	$P = 24$ GPa / depth=670 km
A_1	0.667 (0.652)	0.770 (0.723)
A_2	1.137 (1.139)	1.186 (1.329)
A_3	0.859 (0.914)	0.942 (1.037)

Of special importance for the study of the rupture mechanism in materials is the assessment of elastic anisotropy. To evaluate this property for olivine we calculated the shear anisotropic factors (A_i) (Ravindran et al., 1998). This provides a measure of the degree of anisotropy in the bonding between atoms in different crystal planes. For the {100} shear planes between the ⟨011⟩ and ⟨010⟩ directions, the shear anisotropy factor (A_1) is given by:

$$A_1 = \frac{4C_{44}}{C_{11} + C_{33} - 2C_{13}} \tag{4}$$

For the {010} shear planes between the ⟨101⟩ and ⟨001⟩ directions it assumes the form of

$$A_2 = \frac{4C_{55}}{C_{22} + C_{33} - 2C_{23}} \tag{5}$$

while for the {001} shear planes between the ⟨110⟩ and ⟨010⟩ directions, this factor becomes:

$$A_3 = \frac{4C_{66}}{C_{11} + C_{22} - 2C_{12}}. \tag{6}$$

For an isotropic crystal system all the A-factors assume the same unity value ($A_1 = A_2 = A_3 = 1$), while any departure from 1 represents a measure of the degree of elastic anisotropy. The computed shear anisotropies for olivine are listed in Table 3. The comparison with experimental results from the data of Zha et al. (1998) shows satisfactory agreement over the investigated pressure range. As a general tendency, the high-pressure A-factors exhibit a slightly larger elastic anisotropy than the low-pressure ones. The A_1 shear anisotropy is the most anisotropic factor at both pressures, while the A_3 is the least one. The closeness of the latter parameter to unity at high pressure points to an intrinsic weak anisotropic nature of olivine at the {001}-shear planes. This finding is in line with previous experimental (Mainprice et al., 2005; Raterron et al., 2012) and theoretical (Castelnau et al., 2010) studies, which suggested a weak seismic anisotropy for olivine-rich aggregates that deform by {001}<hk0> slip in the upper mantle below 300 km.

2.1.2. Plastic behaviour

To gain additional insight into the fracture mechanism of the MOW at the subduction zones, the plastic behaviour of olivine was investigated at different pressures. Plastic deformation is here handled within the pure crystal approximation (i.e., no grains and no vacancy concentration-effect) with the aim to monitor the energy released upon rupture of olivine, from the initial breaking of the chemical bonds to the observable seismic energy. Thus, plastic deformation is treated within the mechanism of dislocation glide. Although this approach is in line with several experimental works on the deformation of olivine aggregates (Demouchy et al., 2009; Gasc et al., 2019), we acknowledge that grain boundaries in olivine can amorphize and promote grain-boundary sliding (Samae et al., 2021). While our methodology gives valuable insights into single crystal plasticity, it does not account for the latter behaviour, where a coarser system must be considered in the theoretical modelling.

The single-crystal plasticity was studied by straining the lattice vectors **R** beyond the elastic limit according to the rule **R'=RD**. Here **R'** is a matrix containing the components of the distorted orthorhombic lattice vectors and **D** is the symmetric distortion matrix, which can assume the following volume conserving monoclinic shear strain components:

$$D_4 = \begin{pmatrix} \frac{1}{(1-\delta^2)^{1/3}} & 0 & 0 \\ 0 & \frac{1}{(1-\delta^2)^{1/3}} & \frac{\delta}{(1-\delta^2)^{1/3}} \\ 0 & \frac{\delta}{(1-\delta^2)^{1/3}} & \frac{1}{(1-\delta^2)^{1/3}} \end{pmatrix} \tag{7}$$

$$D_5 = \begin{pmatrix} \frac{1}{(1-\delta^2)^{1/3}} & 0 & \frac{\delta}{(1-\delta^2)^{1/3}} \\ 0 & \frac{1}{(1-\delta^2)^{1/3}} & 0 \\ \frac{\delta}{(1-\delta^2)^{1/3}} & 0 & \frac{1}{(1-\delta^2)^{1/3}} \end{pmatrix} \tag{8}$$

$$D_6 = \begin{pmatrix} \frac{1}{(1-\delta^2)^{1/3}} & \frac{\delta}{(1-\delta^2)^{1/3}} & 0 \\ \frac{\delta}{(1-\delta^2)^{1/3}} & \frac{1}{(1-\delta^2)^{1/3}} & 0 \\ 0 & 0 & \frac{1}{(1-\delta^2)^{1/3}} \end{pmatrix} \tag{9}$$

where δ (Vitos, 2007) represents the distortion parameter (i.e., the geometrical strain). The D_{4-6} shear distortions are the same used in Section 2.1.1 to compute the C_{44}, C_{55}, and C_{66} elastic constants under the elastic limit. However, the difference here stands on the much larger values that take the δ parameter ($0.0 \le \delta \le 0.9$) in order to allow for full stress release upon unit cell distortion. As δ increases, the D_4 matrix operates on the unstrained orthorhombic lattice by decreasing the angle between **b** and **c** lattice vectors. This kind of distortion establishes a slip system that consists of the {010} plane and the ⟨001⟩ direction. The second distortion matrix (D_5) instead shrinks the angle between **a** and **c** lattice vectors and activates the {001}<100> slip system. Similarly, the effect of the D_6 matrix on the orthorhombic lattice diminishes the angle between **a** and **b** vectors and drives the {010}<100> slip system.

The achieved theoretical stress-strain curves are shown in Fig. 5 for two reference pressure values, 5 GPa (red line) and 24 GPa (blue line). The pressure of 5 GPa is here used to simulate the physical conditions of intermediate earthquakes, while that of 24 GPa is used for deep events. Two important features are observed along the complete stress-strain curves. One relates to the maximum amount of stress accumulation permitted by the system under a specific distortion, and this involves the first part of the stress-strain curve (i.e., positive slope). The second feature concerns the descending part of the curve (i.e., negative slope) that gives specific information about the velocity at which stresses are released under different shear distortions. For each of the investigated stress-strain curves (D_{4-6}) we then try to correlate these features to seismological observations, namely, the shape of the Moment Rate Functions (MRF, also called Source Time Functions-STF) of intermediate and deep earthquakes. The MRFs give specific information about the seismic radiated energy released by the earthquake. The way these functions were obtained is accurately illustrated in Section 2.2.

Our main hypothesis is that different slopes on MRFs for deep and intermediate-depth events can be explained in terms of the theoretical stress-strain curves. A direct link is established between the second (descending) part of the theoretical stress-strain curves

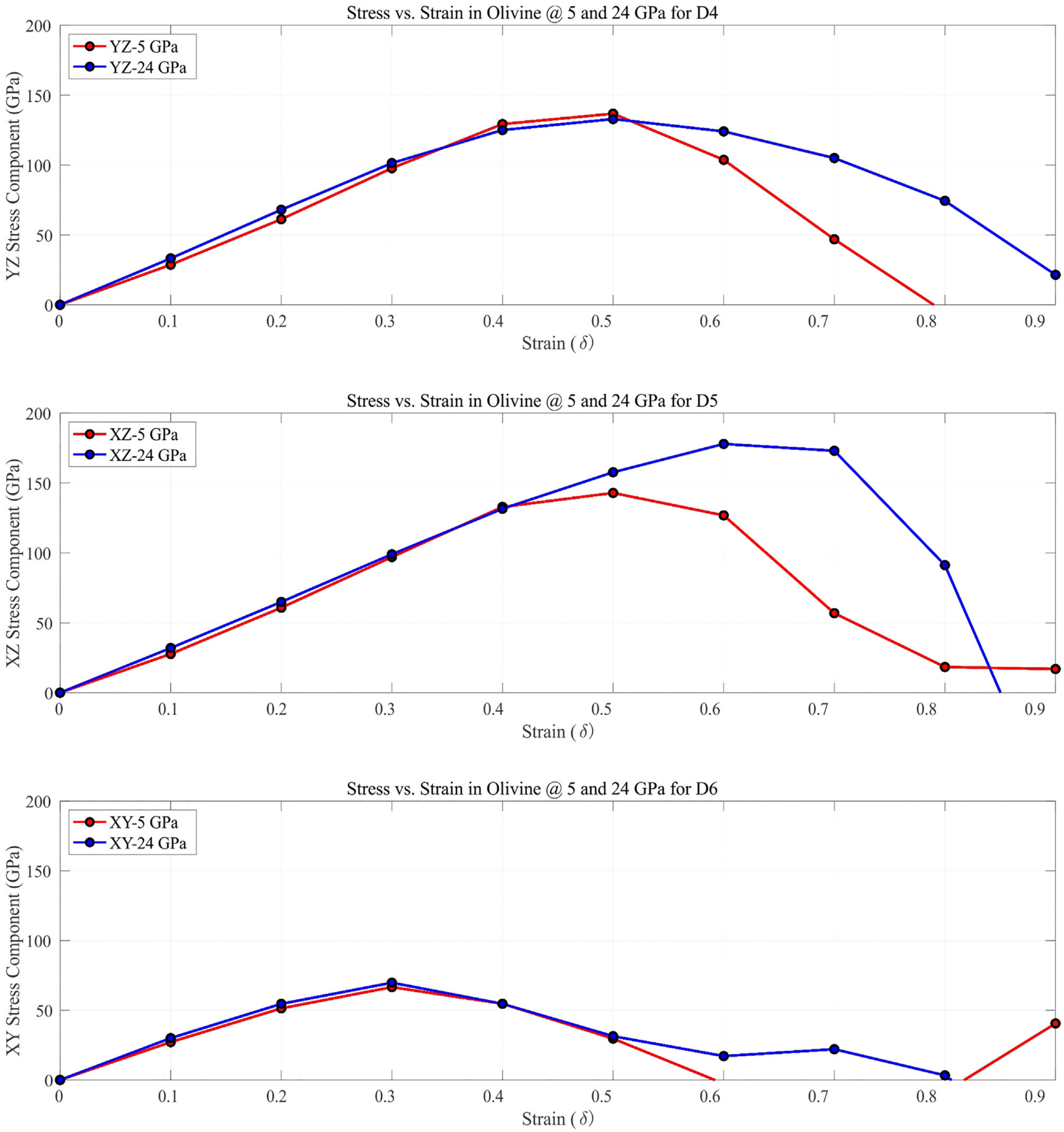

Fig. 5. Theoretical stress-strain curves for the three shear stresses (D_4, D_5 and D_6). For clarity, only the positive stress components (YZ, XZ, and XY) are shown in this figure. Note that when all the six stress components (XX, YY, ZZ, YZ, XZ, XY) are summed up, the resulting theoretical stress drop amounts to 150–200 MPa.

and the first (ascending) part of the MRFs. We here consider that the theoretical model mechanism with the faster stress release (i.e., the stress-strain curve with a larger negative slope) yields a more abrupt start in the MRF curve (i.e., to a larger positive slope). The proposed scenario for the rupture process focuses on the germinal fracture part of the material, where the breaking of chemical bonds develops for the very first time. Bond breaking takes place along a series of adjacency microscopic single-crystal planes that are displaced one next to the other, just like small pieces of a mosaic, to ideally recover the size of the seismic slip plane (Section 4). Although this process represents an approximation to the initial formation of a crack and its subsequent propagation inside the material, it gives a reasonable estimation of the total energy involved in the rupture process. Within such a context, the atomistic rupture mechanism with the fastest rate of stress dissipation should be then manifest seismologically into a more impulsive MRF curve. It is understood that such an assumption holds true only when the chosen event can effectively free the majority of accumulated stresses upon rupture of the material. On the contrary, if crack propagation during fracture gets somehow hindered by other mechanisms, such as crossing different texture domains (e.g., fresh versus consolidated material) or experiencing a change in the type of lattice preferred orientation, then the proposed hypothesis might break down. In this paper, we assume that the selected 43 earthquakes are all fulfilling the above requirement and that the initial rising segment of their MRF curves represents the best zone to look at for atomistic effects.

Let's now analyse in detail the main characteristics of the D_{4-6} mechanisms. The D_6 shear mechanism (bottom of Fig. 5) is the least energetic amongst the three types of shear distortions and it is nearly pressure (depth)-independent. That is, olivine can accumulate the same amount of maximum stress (70 GPa) at both pressures of 5 and 24 GPa. Stresses are also released in a very similar manner (i.e., same velocity), having the two curves at 5 GPa and 24 GPa nearly the same negative slope and shape. Therefore, if we hypothetically assume that an olivine fracture occurs via a D_6 mechanism but at different depths of the same subduction slab, then no differences should be observed in the MRFs of intermediate and very deep earthquakes. However, we have not observed such behaviour in the 43 earthquakes that were analysed in this work, as will be shown below in Section 3. A considerably more energetic shear distortion type is that of D_4 (top of Fig. 5). The maximum amount of stress accumulation for both pressures reach the same value of 133 GPa. Notwithstanding, an important discriminating feature is here found in the second part of the curve, where the velocity of stress release is clearly faster for low-pressure conditions. Hence, if the fracture occurs via the same D_4 mechanism but at different depths, the observed MRFs should differ one from the other. Specifically, the MRFs of intermediate earthquakes are expected to be more abrupt and impulsive. Finally, the D_5 shear-mechanism (middle of Fig. 5) is by far the more energetic amongst the three shear types, and, most important, the two stress-strain curves indicate a diverse dependence with depth. At low-pressure regimes, the maximum amount of stress accumulation is 143 GPa, while at higher pressures this value increases up to 178 GPa. A striking feature is observed in the descending part of the stress-strain curves. The slope changes considerably for the two pressure values indicating a faster stress release for the high-pressure regime. Consequently, if the olivine's fracture occurs via the same D_5 shear-mechanism but at different depths, then deeper events should show a more abrupt start of the MRF curves and a shorter duration of the source time function. Because of the larger amount of stresses that can be accumulated at larger pressures, deeper events should also liberate more energy per unit area of the fracture.

Therefore, differences in the rising part of the MRFs between intermediate and deep earthquakes at a subduction zone must be expected if the fracture occurs via either a D_4 or a D_5 mechanism. Events that are originated at different depths without showing any diversities in their MRFs can be associated with the less energetic and overall, less discriminating D_6 shear mechanism. Although the whole rupture mechanism in olivine is rather complex and should contemplate the here neglected effects of temperature and aggregates (i.e., a multi-scale approach within the visco-plastic modelling), we believe that a detailed atomistic study of the elasto-plastic deformations in solid olivine might help to better understand the controversial source mechanism that is at the origin of the very deep earthquakes.

2.2. Seismic observables

The MRF contains information about the slip's dependence on time and consequently on the rupture process. It may be estimated by using different data or methodologies, such as inversion of body waves at a near field or, back projection, and slip inversion on the fault plane. To compare different earthquakes, possible size differences in the MRFs were accounted for by scaling to a common scalar seismic moment and time duration. To this purpose, we used the methodology proposed by Houston et al. (1998) who define a scaled MRF to a common scalar seismic moment. For an *i-th* event with moment M_0^i, the scaled time t is defined as:

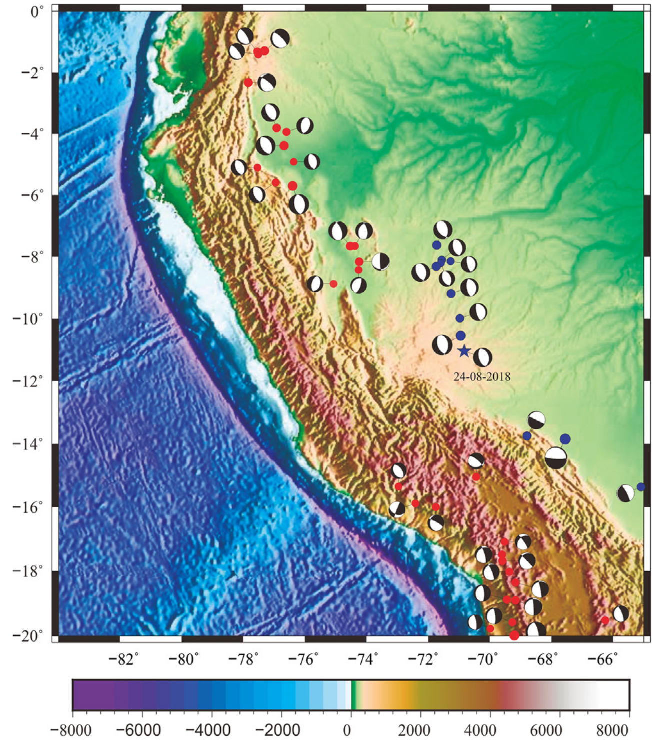

Fig. 6. Focal mechanisms of selected earthquakes taken from SCARDEC (http://scardec.projects.sismo.ipgp.fr/). In red intermediate and in blue deep depth events. The star symbol represents the 24th August 2018 earthquake.

$$t = \left(\frac{M_{0ref}}{M_0^i}\right)^{1/3} \tau, \tag{10}$$

where τ is the unscaled time and M_{0ref} the reference moment which, in our study is 10^{19} Nm. The scaled time t allows comparing the rate of initiation, the relative durations, and the times of moment release. The scaled amplitude u^i_{scaled} defines as follow:

$$u^i_{scaled}(t) = \left(\frac{M_{0ref}}{M_0^i}\right)^{2/3} u^i(\tau), \tag{11}$$

where $u^i(\tau)$ is the unscaled moment. In order to carry out a comparison between the rupture process of intermediate and deep earthquakes, a homogeneous database of the different MRFs is needed.

The seismological data used are the MRFs from a selection of 43 earthquakes taken from the SCARDEC database (Vallée and Douet, 2016; Fig. 6) that occurred in the Peru-Brazil-Bolivia and northern Chile region for the period 1992 to 2018 with $5.7 \leq M_W \leq 8.2$. Amongst them, 31 correspond to intermediate depth foci (100 km $< h <$ 350 km, Table 4) and 12 to deep foci (500 km $< h <$ 700 km, Table 5). The chosen earthquakes are representative of the intermediate and the deep seismicity in this region (Fig. 4). The SCARDEC database uses an extension of the method developed by Vallée et al. (2011). It is a deconvolutive methodology that uses teleseismic body waves to determine the MRF together with other earthquake source parameters (hypocenter, scalar seismic moment, and fault plane orientation). This method automatically provides the optimal and the averaged MRFs.

Since our interest in this study focuses on the global behaviour of the source, we have chosen to monitor the shape of the average MRFs instead of the optimal function. We recall that possible discrepancies between average and optimal MRFs can be due

Table 4
Intermediate-depth earthquakes occurred in the Peru-Brazil-Bolivia and the northern Chile regions (1992–2018) selected from the SCARDEC database (http://scardec.projects.sismo.ipgp.fr/).

Date	Time	Long (°)	Lat (°)	h (km)	M_w
2018/11/1	22:19:51	−69.266	−19.583	106	6.2
2018/1/21	1:06:42	−69.445	−18.881	117	6.3
2017/1/2	13:13:48	−76.368	−4.895	111	5.9
2016/9/10	10:08:20	−76.954	−5.573	122	6.1
2015/3/23	4:51:38	−69.166	−18.353	131	6.4
2012/11/10	14:57:50	−75.071	−8.866	124	6.0
2012/8/2	9:38:30	−74.259	−8.414	150	6.0
2012/6/7	16:03:18	−72.413	−15.877	108	6.1
2012/5/14	10:00:40	−69.591	−17.678	110	6.3
2011/8/24	17:46:11	−74.530	−7.640	150	7.0
2011/6/8	3:06:22	−69.518	−17.083	141	6.0
2011/3/6	12:31:59	−69.360	−18.020	112	6.2
2010/8/12	11:54:15	−77.310	−1.270	208	7.1
2010/5/19	4:15:43	−77.541	−5.083	128	6.0
2009/7/12	6:12:47	−70.440	−15.040	195	6.1
2008/8/26	21:00:36	−74.380	−7.640	153	6.4
2008/7/8	9:13:07	−71.750	−15.990	110	6.1
2007/11/16	3:13:00	−77.840	−2.310	127	6.8
2005/12/23	21:47:28	−77.520	−1.390	188	6.1
2005/9/26	1:55:37	−76.400	−5.680	121	7.5
2005/8/14	2:39:40	−68.980	−19.780	110	5.7
2005/7/26	14:11:36	−72.962	−15.345	103	5.9
2005/6/13	22:44:33	−69.200	−19.990	107	7.7
2001/6/29	18:35:51	−66.250	−19.520	274	6.1
1999/11/30	4:01:53	−69.170	−18.900	134	6.6
1999/8/28	12:40:06	−77.550	−1.290	194	6.3
1998/4/3	22:01:48	−74.240	−8.150	148	6.6
1997/10/28	6:15:17	−76.680	−4.370	113	7.2
1995/5/2	6:06:05	−76.920	−3.790	105	6.7
1994/12/12	7:41:55	−69.600	−17.480	149	6.3
1992/7/13	18:11:33	−76.600	−3.920	110	6.3

Table 5
Deep earthquakes occurred in the Peru-Brazil-Bolivia and the northern Chile regions (1992–2018) selected from the SCARDEC database (http://scardec.projects.sismo.ipgp.fr/).

Date	Time	Long (°)	Lat (°)	h (km)	M_w
2018/8/24	9:04:08	−70.828	−11.035	625	7.0
2016/12/18	13:30:10	−70.970	−9.974	636	6.5
2015/11/26	5:45:18	−71.257	−9.182	611	6.7
2015/11/24	22:45:38	−70.944	−10.537	619	7.5
2011/11/22	18:48:16	−65.090	−15.360	568	6.6
2010/5/24	16:18:29	−71.560	−8.090	581	6.4
2007/7/21	13:27:04	−71.270	−8.130	637	6.0
2003/6/20	6:19:38	−71.720	−7.610	562	7.0
2003/4/27	22:57:44	−71.592	−8.195	570	5.9
2002/10/12	20:09:11	−71.740	−8.300	534	6.9
1997/11/28	22:53:41	−68.790	−13.740	615	6.7
1994/6/9	0:33:16	−67.550	−13.840	664	8.2

to variations in the focal mechanism during the rupture process (Vallée and Douet, 2016). In addition, the way these functions are obtained does not bias the global shape of the STF and makes them insensitive to possible outliers (Vallée and Douet, 2016). Finally, we have applied the Houston et al. (1998) methodology to our selection in order to obtain the averaged moment-scaled time functions (Fig. 7) for intermediate (red curve) and deep (blue curve) depth events. Once the moment-scaled time functions have been obtained for each earthquake, we calculated an averaged MRF for intermediate (100–350 km) and deep (500–700 km) depth events. The number of intermediate and deep depth earthquakes is not the same, being 12 for the former and 31 for the latter, respectively. In both cases, we obtained a mean standard deviation of the order of $\approx 10^{17}$ Nm, which is accurate enough to guarantee a qualitative differentiation of the two curves. The bootstrap methodology was also applied by varying the number of selected events to corroborate that the averaged MRFs do keep the same relative shapes. A clear difference in the rising part of the MRFs curves (i.e., the positive slope) is found for intermediate and deep events, being the latter steeper than the former. This indicates a more abrupt energy liberation and thus a faster dissipation of stresses upon rupture. The way the results of the atomistic modelling of Fig. 5 are bridged to the seismic observables of Fig. 7 is discussed in more detail in the following Section 3.

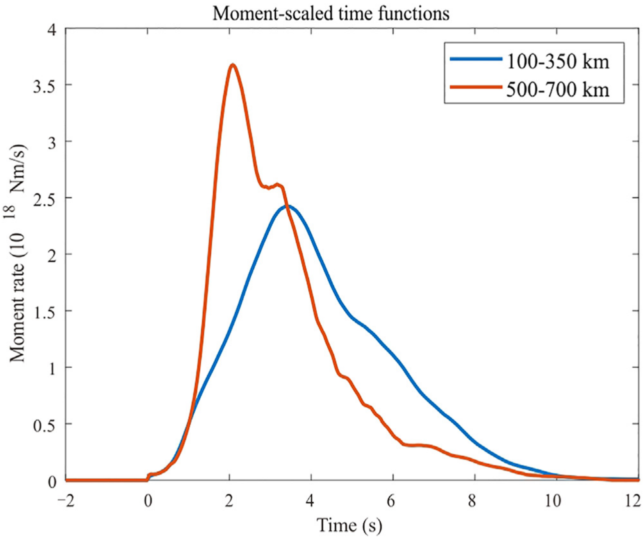

Fig. 7. Average moment-scaled time functions for 12 intermediate (100–350 km) and 31 deep (500–700 km) depth earthquakes.

3. Results

An important contribution to the understanding of the rupture process in subducting zones can be achieved by applying the results of atomistic simulations to the study of the MRFs of intermediate and deep earthquakes. The key anchor point here is the similarity found between the shapes of the averaged moment-scaled time functions (Fig. 7) and the theoretical elasto-plastic response of olivine under pressure (Fig. 5). Such a correlation is further endorsed by an analogous behaviour found in the duration-scaled time functions. In other words, it becomes possible to achieve critical information about the rupture process inside the metastable olivine wedge at the studied region by looking at the outline shape of the observable scaled functions.

The averaged moment-scaled time functions obtained for the two depth bins (100–350 km and 500–700 km) are shown in Fig. 7. If one focuses the attention on the rising part of these curves, that is the time window that starts at zero and ends at the curve maximum, then a different behaviour is found for the two probed depths. Deep events (500–700 km, blue line) have an averaged curve with a steeper slope, to indicate a more abrupt and impulsive energy release for these events. On the contrary, the study of intermediate foci earthquakes (100–350 km, red line) yields an averaged curve with a smaller slope that suggests a more gradual energy liberation at the source. The faster energy-releasing rate found for deep foci events can be attributed to a brittle-like failure in the metastable olivine material, where the discharge of energy results more abruptly than in intermediate earthquakes. As shown in Section 2.1.1, this behaviour can be explained by the pressure hardening effect observed in the computed athermal single-crystal elastic constants.

According to the study of plastic behaviour provided in Section 2.1.2, the D_5 shear-mechanism (middle panel of Fig. 5) is the one that best reproduces the seismic observables. As a matter of fact, this mechanism allows for a larger stress accumulation at high-pressure regimes (i.e., the top of the stress-strain curve) and, most importantly, the shape of stress drop after reaching the maximum point (i.e., descending part of the stress-strain curve) is more abrupt in the high-pressure case. A faster stress release is thus found theoretically for the high-pressure case, which is in line with the seismic observations shown in Fig. 7. Said differently, the second part of the blue curve in Fig. 5 (middle panel) has a more marked negative slope than the red one. The same happens for the blue curve (deep earthquakes) in the first part of Fig. 7, which has a larger positive slope than the red curve (intermediate-depth earthquakes). Because of this observational matching, the D_5 shear-mechanism can be used to explain why deeper events have a more abrupt start in the MRF curves and a shorter duration of the source time function. This is the only shear-strain mechanism whose stress-response fits the observed MRF curves. Indeed, the shape of the descending curves in a D_6 shear-system (bottom panel of Fig. 5) is almost indistinguishable for the two pressure regimes, while the D_4 strain (upper panel of Fig. 5) shows exactly the opposite behaviour observed through the MRF analysis. As a passing by remark, we noticed that all the examined shear mechanisms liberate a different amount of energy depending on the applied external pressure. The greater the depth, the higher the energy freed upon rupture of the material, and this is in line with the increasing C_{ij} values with pressure (Table 2). Specifically, for the D_5 shear-type the energy released at 24 GPa (5.1911×10^{-17} J/cell) almost doubles the one liberated at 5 GPa (2.6800×10^{-17} J/cell).

The selected D_5 distortion matrix involves the gliding of crystal lattice at the {001} slip plane, and this is in good agreement with the more general {001}<hk0> slip system, that was previously targeted (Mainprice et al., 2005; Castelnau et al., 2010; Raterron et al., 2012) as the dominant deformation mechanism for olivine at depths >65 km. It is worth mentioning that the main novelty introduced in this work consists in having focused the search for the shear system that best matches the MRF curves on the unloading stage of the theoretical stress-strain curves. Thus, the quest for a characteristic stress-strain feature was conducted at the descending part of the curve rather than inspecting the ascending loading stage, which is what has been done in previous studies. The reason for such a choice stands behind the fact that the way stresses are released after fracture is more directly connected to how energy is freed at the source during an event rather than to the way stresses are accumulated before fracture. Nonetheless, it is gratifying to see that different methodologies have led to the same atomistic scenario for olivine under shear stress conditions.

Besides the attempt made to understand the mechanism of energy release during an earthquake, efforts were also directed to quantify the total amount of energy freed during the rupture process. In this case, the radiated seismic energy (E_R) is here used as a reference seismic observable for theoretical estimations. The E_R is defined as the wave energy that is transmitted to infinity when an earthquake originated inside an infinite perfectly elastic medium occurs without loss of energy (Haskell, 1964). Several authors have suggested different methods to obtain the radiated seismic energy (Boatwright, 1980; Vassiliou and Kanamori, 1982; Venkataraman and Kanamori, 2004). Here we have estimated the E_R for the deep earthquake that occurred on the 24th August 2018 ($M_w = 7$; blue star in Fig. 6) by assuming a point source and using the relationship proposed by Venkataraman and Kanamori (2004):

$$E_R = \left(\frac{1}{15\pi^2 \rho \alpha^5} + \frac{1}{10\pi^2 \rho \beta^5} \right) \int_0^\infty \omega^2 \left| \dot{M}_0(\omega) \right|^2 d\omega \qquad (12)$$

where the first two terms represent the P-wave and S-wave contributions, being α the P-wave velocity, β the S-wave velocity and ρ the density in the source region. This mathematical relationship allows us to calculate the radiated seismic energy at each seismic station from the known source spectrum [$\dot{M}_0(\omega)$]. We have selected 24 teleseismic stations that are not nodal and whose records have amplitude spectra with a signal-to-noise ratio greater than 1.25. The displacement amplitude spectra were corrected by the radiation pattern, the anelastic attenuation ($t^* = 0.3$ s; Ye et al., 2013; Poli and Prieto, 2016), the geometrical spreading, and the free surface. To compute the radiation pattern and the geometrical spreading, we have estimated the focal mechanism from slip inversion of body waves at teleseismic distances (Kikuchi and Kanamori, 1991). We have used a density $\rho = 3.98$ g/cm^3, P- and S-wave velocity $\alpha = 10.21$ km/s and $\beta = 5.54$ km/s, obtaining a mean radiated seismic energy of 6×10^{15} J. This value agrees with the results obtained by other authors for earthquakes of the same region (Ruiz et al., 2017).

4. Discussion

From an atomistic point of view, the total energy liberated upon brittle failure of a bulk (metastable) olivine can be computed by using the maximum energy value of one of the stress-strain curves shown in Fig. 5 and multiplying it by a normalizing surface factor n_o. This factor allows recovering the area of the macroscopic seismic slip plane ($S = 1726$ km^2, obtained from the slip inversion of the 24th August 2018 earthquake) by repeating many times the microscopic unit cell plane that slips under the effect of a given shear. For the three types of shear distortions considered for olivine (D_4, D_5, and D_6) these energy maxima correspond to 183.93 eV, 324.03 eV, and 43.92 eV, respectively. However, since the D_5 shear-mechanism is the one that best explains the MRF analysis, we then used this energy to address the rupture of olivine along the microscopic {001} plane with a surface area of $S_{\{001\}} = 5.7806 \times 10^{-25}$ km^2. Therefore, $S_{\{001\}}$ represents the area of the atomistic {001} shear plane that is theoretically measured right before the breaking of chemical bonds upon distortion of the crystal. A normalizing surface factor ($n_o = S/S_{\{001\}}$) of 2.9858×10^{27} was computed with the aim to extend this microscopic rupture to the observable seismic slip plane of 1726 km^2, leading to a reference energy E_o of 1.6362×10^{11} J. This value represents the macroscopic energy release upon the breaking of chemical bonding along the n_o {001} planes during the formation of two separated surfaces.

However, this is not the only energy portion that can be liberated during rupture. For a macroscopic solid we need to further consider the releasing of a considerable amount of energy coming from the distorted yet unbroken layers of material, which are lying immediately above and below the line of cut (characterized by the reference energy E_o). Such deformed layers will not experience the same bond-breaking mechanism that occurs at the line of fracture. Instead, their chemical bonds will behave as a sort of loaded springs that will promptly liberate their energies to restore back their equilibrium positions. Their degree of distortion, stress accumulation, and therefore the amount of liberated energy, depends on the distance from the reference plane with energy E_o. To account for such a complex macroscopic scenario within a simplified picture, we made use of the layered model shown in Fig. 8 to represent the rupture process of an earthquake, where the energetic of ten different layers ($E_o \ldots E_9$) with thickness d was considered both above and below the plane of rupture. When all layers assume a common thickness of 50 cm and the amount of released energy decreases linearly with distance (i.e., layer E_1 liberates 90% of E_o, E_2 80% and on so on), the total freed energy reaches 1.5980×10^{21} J. By changing the layer thickness down to 10 cm, this energy only lowers by one order of magnitude. This energy value can be considered as an atomistic approximation to the total rupture energy $E_T = E_R + E_F + E_G$ (Kanamori and Brodsky, 2004;

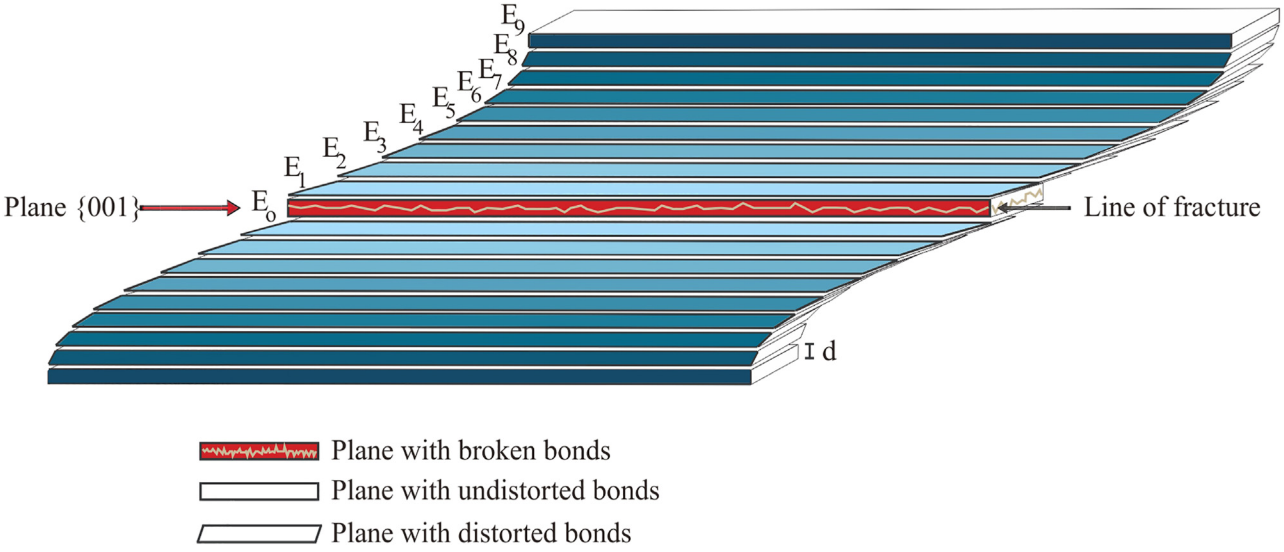

Fig. 8. Atomistic layered model for a rupture along the {001} plane. For the sake of simplicity, we assigned the same thickness *d* to each layer. The plane with reference energy E_o incorporates the line of fracture (i.e., two surfaces are generated by breaking of chemical bonding), while those immediately above and below are unbroken planes having different degrees of chemical bonding distortion. The grade of such a deformation diminishes linearly with the distance from E_o. Undamaged planes whose chemical bonding are not affected by the line of fracture at E_o begins at plane with energy E_9.

Kanamori and Rivera, 2006), where E_R is the radiated seismic energy, E_F is the energy dissipated on the frictional process (mostly heat loss) and E_G the fracture energy required to generate damage (deformations) around the fault. This represents an important achievement because although E_R and E_G can be estimated from seismic data, E_F cannot be measured directly from seismic wave observations. When comparing this theoretical total energy value ($E_T = E_R + E_F + E_G \approx 10^{21}$ J) to the observed mean radiated seismic energy ($E_R \approx 10^{15}$ J) for the deep earthquake that occurred on the 24th of August 2018 ($\mathrm{M_w} = 7$), a difference of six orders of magnitudes is found. This indicates that the sum of $E_F + E_G$ assumes a rather large value within the whole energy balance. Although the separation between E_F and E_G is not always clear cut, it is tempting to state that a large quantity of energy gets lost by the seismic waves during the way path to the seismometer. In seismology, a common way to define the fraction of total energy that is radiated into seismic waves (Aki and Richards, 1980; Shearer, 2019) is through the seismic efficiency factor (η):

$$\eta = \frac{E_R}{E_R + E_G + E_F} \tag{13}$$

Note that the seismic efficiency η should not be confused with the radiation efficiency η_R. The first is the ratio of E_R to the total potential energy change, while the latter it is a different quantity that includes the ratio of E_R to the available potential energy (Ye et al., 2016b). In this work, we use the definition of seismic efficiency because our *ab initio* methodology provides direct access to the total energy of rupture.

The estimation of η is rather challenging from seismic data because it strongly depends upon the poorly constrained absolute stress level on the fault. Only in the extreme case, when the earthquake releases all the stress on the fault, this parameter can be computed by assuming $E_F = 0$. The seismic efficiency depends on the source parameters and can assume different values for shallow, intermediate, and deep earthquakes. For instance, from laboratory experiments and mining-induced events, McGarr (1994) hypothesized $\eta \leq 0.06$ for small events ($1.9 \leq M \leq 3.3$). Similarly, for the strong and deep 1994 Bolivian earthquake ($\mathrm{M_w} = 8.3$ and 636 km depth), Kanamori et al. (1998) suggested that the maximum seismic efficiency was 0.04. Bearing in mind these values, we calculated the efficiency factor for the deep earthquake that occurred on the 24th August 2018 ($\mathrm{M_w} = 7$) by using the atomistic total rupture energy and the observed mean radiated seismic energy to obtain:

$$\eta = \frac{E_R}{E_T} \approx \frac{10^{15}\ \mathrm{J}}{10^{21}\ \mathrm{J}} \approx 10^{-6} \tag{14}$$

The η value now lowers by four orders of magnitudes. This raises firm doubts about the commonly accepted energy budget involved in intermediate and deep depth earthquakes (Prieto et al., 2013) and, more generally, generates ambiguity about the value of the efficiency factor that is normally handled in seismology. Such a coefficient could be orders of magnitudes lower than the frequently accepted values. Besides the uncertainty on the E_F energy term, further disagreements could arise from the source model that is used to obtain the radiated seismic energy. In fact, the seismic rupture model has been proved to be reasonable for shallow earthquakes but could lead to an important shortcoming description in intermediate and deep foci events, as shown by those of the Peruvian-Brazilian subduction zone that we investigated in this work.

Additionally, seismological estimations of the stress drop might be also biased by the uncertainly in the observed radiated energy. If a considerable portion of the energy liberated by an event gets lost during the path toward the seismometer, then the observed E_R at the Earth's surface could lead to a shortcoming estimation of the stress drop. For deep earthquakes in the Peru region, several authors have obtained a seismic stress drop that ranges between 1.0 and 19 MPa (Poli and Prieto., 2016; Ye et al., 2016b; Ruiz et al., 2017). Our stress-strain model in Fig. 5 provides a local stress drop of 150–200 MPa, which is roughly ten times larger than the seismic values found for this region. Nevertheless, in seismology, it is well-known that the local stress drop obtained from very detailed kinematic source inversions can be much larger than the one achieved through an average study of the rupture process (Noda et al., 2013; Poli and Prieto, 2016). For certain deep events very high values of stress drop are sometimes observed. As such, Prieto et al. (2017) have found for an $\mathrm{M_w} = 4.8$ earthquake at

75 km depth a stress drop ranging from 60 MPa to 300 MPa, which agrees rather well with our theoretical estimations.

5. Conclusions

The occurrence of an earthquake is commonly explained by the building-up of stresses, their nucleation, and further release within fault zones. When the accumulated stress overcomes the resistance of the material, then fracture occurs by a sudden release of energy that partly propagates outwardly in the form of elastic (seismic) waves. From a classical source theory scenario, the energy balance of an earthquake contemplates two main energetic sets, which can be separated into local and non-local energy terms. The first set refers to the local energy that is explicitly involved in the rupture of the material and incorporates the fracture energy, the energy lost by friction during plastic processes, and the heat loss at the source. The second set encloses the radiated seismic energy and its frictional dissipation, which are non-local energy components associated with the transmission of waves all the way through a non-perfect elastic medium (i.e., the earth's interior), from the source of the earthquake to the earth's surface. When attempting to compute the energy budget of an earthquake from the recorded seismic waves, it is only possible to calculate in detail the non-local seismic energy radiated by the earthquake, while the local friction, thermal and fracture energies can only be approximated by making use of the so-called efficiency factor. Until now, the proposed earthquake fracture models are classical mechanical models which do not consider the properties of the material at its microscopic or atomic level.

Our study starts from the hypothesis that within the cold olivine scenario, the atomistic transformational faulting is the principal mechanism in both deep and intermediate-depth earthquakes. We found that a common D_5 shear-mechanism, that corresponds to the {001}<100> slip system, could be responsible for the same source mechanism of both intermediate and deep depth events. This has been applied to the study of 43 intermediate and deep earthquakes at the Peruvian-Brazilian subduction zone. Results were achieved by conducting a multi-disciplinary study with the intent to bridge the available seismic observables (MRF analysis) to the theoretical atomistic calculations. The uniqueness of this work lodge from the searching of the shear system that best matches the seismic observables by inspecting the descending part of the stress-strain curve rather than focusing the attention on the loading stage. The D_5-based atomistic rupture model indicates that the amount of energy released during fracture increases with depth. To this context, it seems logical that deep earthquakes require more energy to break the material, even though they radiate the same seismic energy of intermediate events. The amount of seismic strain release could be further connected to the type of atomistic mechanism involved in the rupture process. According to our results, the strain drop invariance found by Vallée (2013) for shallow and deep earthquakes can be explained by a common shear rupture mechanism that conserves at different depths. This advances the hypothesis that an identical physical mechanism, such as plastic instability (Roberts and Turcotte, 2000), could be accountable for all earthquakes.

The proposed model is certainly another approximation to the complex rupture process, just like the other mechanical models, but using an atomistic point of view. Test calculations were performed for the deep earthquake that occurred on the 24th of August 2018 ($M_w = 7$) to give rupture energy of 6 orders of magnitudes larger than the observable radiated seismic energy. Although it is somehow reasonable that this energy is larger than the one achieved with simple mechanical models (kinematic or dynamic), this indicates that there might be space to redefine the commonly accepted order of magnitude of the seismic efficiency. The latter parameter normally spans between 10^{-2} and 0.22 (Spottiswoode and McGarr, 1975; Kikuchi, 1992; Wang, 2004), while we compute a number that is clearly much lower ($\eta \approx 10^{-6}$). This opens to the possibility that the total energy freed by an earthquake is much larger than initially thought, and/or most of it gets lost before reaching the earth's surface. Herewith, we are not inferring that the proposed model performs better than the mechanical ones, but that it is simply of another type and overall based on different approximations. With the aim to stimulate research activities in this field, the problem of energy balance was tackled from an unusual microscopic (atomistic) perspective to assess macroscopic seismic observables. The obtained information about fine-scale physics and structure of the MOW-based materials can be further used as a first step towards the complex upscale to the continuum system, where grains and defects can be explicitly treated inside the material.

Declaration of Competing Interest

The authors declare that they have no known competing financial interests or personal relationships that could have appeared to influence the work reported in this paper.

Acknowledgments

This work has been partially supported by the Spanish Ministry of Economy and Competitiveness (Projects CGL2017–86070-R and PID2021-122662OB-I00) and by the "*Proyecto de Investigación Santander-UCM*" (PR44/21- 366 29929). The authors thank Prof. H. Kanamori, Prof. R. Madariaga, and Prof. L. Rivera for their fruitful discussions and comments.

MM designed the study, carried out *ab initio* calculations, wrote the manuscript, prepared part of the Tables and Figures, participated in data analysis and interpretation of results. CL carried out the seismic analysis, drafted the seismic section, prepared part of the Tables and Figures, and participated in data analysis. EB designed the study, carried out the seismic analysis, participated in the interpretation of results, and critically revised the manuscript. AU designed the study, participated in the interpretation of results, and critically revised the manuscript. JSV carried out *ab initio* calculations and participated in the interpretation of results. HT collected seismic data, participated in data analysis and interpretation of results. CP carried out the seismic analysis and critically revised the manuscript. All authors gave final approval for publication and agree to be held accountable for the work performed therein.

References

Aki, K., Richards, P.G., 1980. Quantitative Seismology: Theory and Methods. W.H. Freeman, San Francisco, California Vol. I and II.

Anderson, O.L., 1963. A simplified method for calculating Debye temperature from elastic constants. J. Phys. Chem. Solids 24, 909. doi:10.1016/0022-3697(63)90067-2.

Angermann, D., Klotz, J., Reigber, C., 1999. Space-geodetic estimation of the Nazca-South America Euler vector. Earth Planet. Sci. Lett. 171 (3), 329–334. doi:10.1016/S0012-821X(99)00173-9.

Argus, D.F., Heflin, M.B., 1995. Plate motion and crustal deformation estimated with geodetic data from the global positioning system. Geophys. Res. Lett. 22 (15), 1973–1976. doi:10.1029/95GL02006.

Baur, W.H., 1972. Computer-simulated crystal-structures of observed and hypothetical Mg_2SiO_4 polymorphs of low and high-density. Am. Minerol. 57, 709.

Bina, C.R., 1991. Mantle discontinuities. U.S. Natl. Rep. IUGG, 1987- 1990. Rev. Geophys. 29, 783–793. doi:10.1002/rog.1991.29.s2.783.

Bishop, B.T., Beck, S.L., Zandt, G., Wagner, L., Long, M., Antonijevic, S.K., Tavera, H., 2017. Causes and consequences of flat-slab subduction in southern Peru. Geosphere 13 (5), 1392–1407. doi:10.1130/GES01440.1.

Blöchl, P.E., 1994. Projector augmented-wave method. Phys. Rev. B 50, 17953. doi:10.1103/PhysRevB.50.17953.

Boatwright, J., 1980. A spectral theory for circular seismic sources; simple estimates of source dimension, dynamic stress drop, and radiated seismic energy. Bull. Seismol. Soc. Am. 70 (1), 1–27.

Brodholt, J., Patel, A., Refson, K., 1996. An ab initio study of the compressional behavior of forsterite. Am. Minerol. 81, 257–260.

Cahill, T., Isacks, B.L., 1992. Seismicity and shape of the subducted Nazca plate. J. Geophys. Res. 97 (B12), 17503–17529. doi:10.1029/92JB00493.

Castelnau, O., Cordier, P., Lebensohn, R.A., Merkel, S., Raterron, P., 2010. Microstructures and rheology of the earth's upper mantle inferred from a multiscale approach. C.R. Phys. 11, 304–315. doi:10.1016/j.crhy.2010.07.011.

Chen, C., Liu, L., Wen, Y., Jiang, Y., Chen, L., 2019. Elastic properties of orthorhombic YBa$_2$Cu$_3$O$_7$ under pressure. Crystals 9, 497–509. doi:10.3390/cryst9100497.

Chlieh, M., Perfettini, H., Tavera, H., Avouac, J.P., Remy, D., Nocquet, J.M., Rolandone, F., Bondoux, F., Gabalda, G., Bonvalot, S., 2011. Interseismic coupling and seismic potential along the Central Andes subduction zone. J. Geophys. Res. 116 (B12405). doi:10.1029/2010JB008166.

DeMets, C., Gordon, R.G., Argus, D.F., Stein, S., 1990. Current plate motions. Geophys. J. Int. 101 (2), 425–478. doi:10.1111/j.1365-246X.1990.tb06579.x.

DeMets, C., Gordon, R.G., Argus, D.F., Stein, S., 1994. Effect of recent revisions to the geomagnetic reversal time scale on estimates of current plate motions. Geophys. Res. Lett. 21 (20), 2191–2194. doi:10.1029/94GL02118.

DeMets, C., Gordon, R.G., Argus, D.F., 2010. Geologically current plate motions. Geophys. J. Int. 181 (1), 1–80. doi:10.1111/j.1365-246X.2009.04491.x.

Demouchy, S., Schneider, S.E., Mackwell, S.J., Zimmerman, M.E., Kohlstedt, D.L., 2009. Experimental deformation of olivine single crystals at lithospheric temperatures. Geophys. Res. Lett. 36, L04304. doi:10.1029/2008GL036611.

Ferrand, T.P., Hilairet, N., Incel, S., Deldicque, D., Labrousse, L., Gasc, J., Renner, J., Wang, Y., Green, H.W., Schubnel, A., 2017. Dehydration-driven stress transfer triggers intermediate-depth earthquakes. Nat. Commun. 8, 15247. doi:10.1038/ncomms15247.

Ferreira, F., Hansen, L.N., Marquardt, K., 2021. The effect of grain boundaries on plastic deformation of olivine. J. Geophys. Res Solid Earth 126. doi:10.1029/2020JB020273, e2020JB020273.

Fish, J., Wagner, G.J., Keter, S., 2021. Mesoscopic and multiscale modelling in materials. Nat. Mater. 20, 774–786. doi:10.1038/s41563-020-00913-0.

Frohlich, C., 1989. The nature of deep-focus earthquakes. Annu. Rev. Earth Planet. Sci. 17, 227. doi:10.1146/Annurev.Ea.17.050189.001303.

Frohlich, C., Davis, S.D., 1993. Teleseismic b-values; Or, much ado about 1.0. J. Geophys. Res. 98, 631–644. doi:10.1029/92JB01891.

Frohlich, C., 2006. Deep Earthquakes. Cambridge University Press.

Gasc, J., Demouchy, S., Barou, F., Koizumi, S., Cordier, P., 2019. Creep mechanisms in the lithospheric mantle inferred from deformation of iron-free forsterite aggregates at 900–1200°C. Tectonophysics 761, 16–30. doi:10.1016/j.tecto.2019.04.009.

Green, H., Burnley, P., 1989. A new self-organizing mechanism for deep-focus earthquakes. Nature 341, 733–737. doi:10.1038/341733a0.

Green, H.W., Houston, H., 1995. The mechanics of deep earthquakes. Annu. Rev. Earth Planet. Sci. 23, 169–214. doi:10.1146/annurev.ea.23.050195.001125.

Guatteri, M., Spudich, P., 1998. Coseismic temporal changes of slip direction: the effect of absolute stress on dynamic rupture. Bull. Seismol. Soc. Am. 88, 777–789.

Gutscher, M.A., Maury, R., Eissen, J.P., Bourdon, E., 2000. Can slab melting be caused by flat subduction? Geology 28 (6), 535–538. doi:10.1130/0091 7613(2000)28<535:CSMBCB>2.0.CO;2.

Hacker, B.R., Peacock, S.M., Abers, G.A., Holloway, S.D., 2003. Subduction factory - 2. Are Intermediate-depth earthquakes in subducting slabs linked to metamorphic dehydration reactions? J. Geophys. Res. 108, 2030. doi:10.1029/2001JB001129.

Haskell, N.A., 1964. Total energy and energy spectral density of elastic wave radiation from propagating faults. Bull. Seismol. Soc. Am. 54 (6A), 1811–1841.

Hayes, G.P., Wald, D.J., Johnson, R.L., 2012. Slab1. 0: a three-dimensional model of global subduction zone geometries. J. Geophys. Res. Solid Earth 117 (B1). doi:10.1029/2011JB008524.

Hill, R., 1952. The elastic behaviour of a crystalline aggregate. Proc. Phys. Soc. Lond. 65, 349–355. doi:10.1088/0370-1298/65/5/307.

Hohenberg, P., Kohn, W., 1964. Inhomogeneous electron gas. Phys. Rev. 136, B864. doi:10.1103/PhysRev.136.B864.

Houston, H., Williams, Q., 1991. Fast rise times and the physical mechanism of deep earthquakes. Nature 352, 520–522. doi:10.1038/352520a0.

Houston, H., 1993. The non -double-couple component of deep earthquakes and the width of the seismogenic zone. Geophys. Res. Lett. 20, 1687–1690. doi:10.1029/93GL01301.

Houston, H., Vidale, J.E., 1994. The temporal distribution of seismic radiation during deep earthquake rupture. Science 265, 771–774. doi:10.1126/science.265.5173.771.

Houston, H., Benz, H.M., Vidale, J.E., 1998. Time functions of deep earthquakes from broadband and short-period stacks. J. Geophys. Res. 103, 29895–29913. doi:10.1029/98JB02135.

Houston, H., 2001. Influence of depth, focal mechanism, and tectonic setting on the shape and duration of earthquake source time functions. J. Geophys. Res. 106, 11137–11150. doi:10.1029/2000JB900468.

Houston, H., 2007. Deep earthquakes. In: Treatise On Geophysics Vol. 1 (ed G. Schubert) 321–350, Elsevier.

Ibrahim, A.M., 1988. Ion-beam mixing of metals and debye temperature. Nucl. Instrum. Methods Phys. Res. B 34, 135. doi:10.1016/0168-583X(88)90376-X.

Jiang, G.M., Zhao, D.P., Zhang, G.B., 2008. Seismic evidence for a metastable olivine wedge in the subducting Pacific slab under Japan Sea. Earth Planet. Sci. Lett. 270, 300–307. doi:10.1016/j.epsl.2008.03.037.

Kanamori, H., Anderson, D.L., Heaton, T.H., 1998. Frictional melting during the rupture of the 1994 Bolivian earthquake. Science 279, 839–842. doi:10.1126/science.279.5352.839.

Kanamori, H., Brodsky, E.E., 2004. The physics of earthquakes. Rep. Prog. Phys. 67, 1429–1496. doi:10.1088/0034-4885/67/8/R03.

Kanamori, H., Rivera, L., 2006. Energy partitioning during an earthquake. In: Abercro, R., McGair, A., Kanamori, H., di Toro, G. (Eds.), Earthquakes: Radiated Energy and the Physics of Faulting, Geophysical Monograph Series 170. American Geophysical Union, Washington, pp. 3–13. doi:10.1029/170GM03.

Katsura, T., Ito, E., 1989. The system Mg$_2$SiO$_4$-Fe$_2$SiO$_4$ at high pressures and temperatures: precise determination of stabilities of olivine, modified spinel, and spinel. J. Geophys. Res. 94, 15663–15670. doi:10.1029/JB094iB11p15663.

Kawakatsu, H., Yoshioka, S., 2011. Metastable olivine wedge and deep dry cold slab beneath southwest Japan. Earth Planet. Sci. Lett. 303, 1–10. doi:10.1016/j.epsl.2011.01.008.

Kelemen, P.B., Hirth, G., 2007. A periodic shear-heating mechanism for intermediate-depth earthquakes in the mantle. Nature 446, 787–790. doi:10.1038/nature05717.

Kendrick, E., Bevis, M., Smalley Jr,, R., Brooks, B., Vargas, R.B., Laurıa, E., Fortes, L.P.S., 2003. The Nazca–South America Euler vector and its rate of change. J. S. Am. Earth Sci. 16 (2), 125–131. doi:10.1016/S0895-9811(03)00028-2.

Kim, Y., Clayton, R.W., 2015. Seismic properties of the Nazca oceanic crust in southern Peruvian subduction system. Earth Planet. Sci. Lett. 429, 110–121. doi:10.1016/j.epsl.2015.07.055.

Kikuchi, M., Kanamori, H., 1991. Inversion of complex body waves-III. Bull. Seismol. Soc. Am. 81 (6), 2335–2350.

Kikuchi, M., 1992. Strain drop and apparent strain for large earthquakes. Tectonophys 211, 107–113. doi:10.1016/0040-1951(92)90054-A.

Kirby, S.H., Durham, W.B., Stern, L.A., 1991. Mantle phase changes and deep-earthquake faulting in subducting lithosphere. Science 252, 216–225. doi:10.1126/science.252.5003.216.

Kirby, S.H., Stein, S., Okal, E.A., Rubie, D.C., 1996. Metastable mantle phase transformations and deep earthquakes in subducting oceanic lithosphere. Rev. Geophys. 34, 261–306. doi:10.1029/96RG01050.

Kohn, W., Sham, L.J., 1965. Self-consistent equations including exchange and correlation effects. Phys. Rev. 140, A1133. doi:10.1103/PhysRev.140.A1133.

Kresse, G., Furthmüller, J., 1996. Efficient iterative schemes for ab initio total-energy calculations using a plane-wave basis set. Phys. Rev. B 54, 11169. doi:10.1103/PhysRevB.54.11169.

Kresse, G., Joubert, D., 1999. From ultrasoft pseudopotentials to the projector augmented-wave method. Phys. Rev. B 59, 1758. doi:10.1103/PhysRevB.59.1758.

Le Page, Y., Saxe, P., 2001. Symmetry-general least-squares extraction of elastic coefficients from ab initio total energy calculations. Phys. Rev. B 63, 174103. doi:10.1103/PhysRevB.63.174103.

Le Page, Y., Saxe, P., 2002. Symmetry-general least-squares extraction of elastic data for strained materials from ab initio calculations of stress. Phys. Rev. B 65, 104104. doi:10.1103/PhysRevB.65.104104.

Lim, H., Kim, Y., Clayton, R.W., Thurber, C.H., 2018. Seismicity and structure of Nazca Plate subduction zone in southern Peru. Earth Planet. Sci. Lett. 498, 334–347. doi:10.1016/j.epsl.2018.07.014.

Liu, L., Zhang, J.S., 2015. Differential contraction of subducted lithosphere layers generates deep earthquakes. Earth Planet. Sci. Lett. 421, 98–106. doi:10.1016/j.epsl.2015.03.053.

Ma, Y., Clayton, R.W., 2015. Flat slab deformation caused by interplate suction force. Geophys. Res. Lett. 42 (17), 7064–7072. doi:10.1002/2015GL065195.

Mainprice, D., Tommasi, A., Couvy, H., Cordier, P., Frost, D.J., 2005. Pressure sensitivity of olivine slip systems and seismic anisotropy of Earth's upper mantle. Nature 433, 731–733. doi:10.1038/nature03266.

Marton, F., Bina, C.R., Stein, S., Rubie, D.C., 1999. Effects of slab mineralogy on subduction rates. Geophys. Res. Lett. 26, 119–122. doi:10.1029/1998GL900230.

Mattesini, M., Matar, S.F., 2002. Density-functional theory investigation of hardness, stability, and electron-energy-loss spectra of carbon nitrides with C$_{11}$N$_4$ stoichiometry. Phys. Rev. B 65, 075110. doi:10.1103/PhysRevB.65.075110.

McGarr, A., 1994. Some comparisons between mining-induced and laboratory earthquakes. Pure Appl. Geophys. 142 (3-4), 467–489. doi:10.1007/BF00876051.

Meade, C., Jeanloz, R., 1991. Deep-focus earthquakes and recycling of water into the earth's mantle. Science 252, 68–72. doi:10.1126/science.252.5002.68. MedeA is a trademark of Materials Design Inc. [http://www.materialsdesign.com]

Milstein, F., Hill, R., 1979. Divergences among the born and classical stability criteria for cubic crystals under hydrostatic loading. Phys. Rev. Lett. 43, 1411–1413. doi:10.1103/PhysRevLett.43.1411.

Minster, J.B., Jordan, T.H., 1978. Present-day plate motions. J. Geophys. Res. Solid Earth 83 (B11), 5331–5354. doi:10.1029/JB083iB11p05331.

Momma, K., Izumi, F., 2011. VESTA 3 for three-dimensional visualization of crystal, volumetric and morphology data. J. Appl. Crystallogr. 44, 1272–1276. doi:10.1107/S0021889811038970.

Monkhorst, H.J., Pack, J.D., 1976. Special points for Brillouin-zone integrations. Phys. Rev. B 13, 5188. doi:10.1103/PhysRevB.13.5188.

Moore, P.B., Smith, J.V., 1969. High pressure modification of Mg$_2$SiO$_4$-crystal structure and crystallochemical and geophysical implications. Nature 221, 653. doi:10.1038/221653a0.

Noda, H., Lapusta, N., Kanamori, H., 2013. Comparison of average stress drop measures for ruptures with heterogeneous stress change and implications for earthquake physics. Geophys. J. Int. 193, 1691–1712. doi:10.1093/gji/ggt074.

Norabuena, E., Leffler-Griffin, L., Mao, A., Dixon, T., Stein, S., Sacks, I.S., Ellis, M., 1998. Space geodetic observations of Nazca-South America convergence across the central Andes. Science 279 (5349), 358–362. doi:10.1126/science.279.5349.358.

Norabuena, E.O., Dixon, T.H., Stein, S., Harrison, C.G., 1999. Decelerating Nazca-South America and Nazca-Pacific plate motions. Geophys. Res. Lett. 26 (22), 3405–3408. doi:10.1029/1999GL005394.

Nye, J.F., 1985. Physical Properties of Crystals: Their Representation By Tensors and Matrices. Oxford University Press, New York ISBN 0198511655.

Ogawa, M., 1987. Shear instability in a viscoelastic material as the cause of deep focus earthquakes. J. Geophys. Res. 92, 13801–13810. doi:10.1029/JB092iB13p13801.

Ohuchi, T., Lei, X.L., Ohfuji, H., Higo, Y.J., Tange, Y., Sakai, T., Fujino, K., Irifune, T., 2017. Intermediate-depth earthquakes linked to localized heating in dunite and harzburgite. Nat. Geosci. 10, 771–776. doi:10.1038/NGEO3011.

Ohuchi, T., Lei, X.L., Higo, Y.J., Tange, Y., Sakai, T., Fujino, K., 2018. Semi-brittle behavior of wet olivine aggregates: the role of aqueous fluid in faulting at upper mantle pressures. Contrib. Mineral. Petrol. 173, 88. doi:10.1007/s00410-018-1515-9.

Peacock, S.M., Wang, K., 1999. Seismic consequences of warm versus cool subduction metamorphism: examples from southwest and northeast Japan. Science 286, 937–939. doi:10.1126/science.286.5441.937.

Perdew, J.P., Burke, K., Ernzerhof, M., 1996. Generalized gradient approximation made simple. Phys. Rev. Lett. 77, 3865. doi:10.1103/PhysRevLett.77.3865.

Phillips, K., Clayton, R.W., Davis, P., Tavera, H., Guy, R., Skinner, S., Aguilar, V., 2012. Structure of the subduction system in southern Peru from seismic array data. J. Geophys. Res. Solid Earth 117 (B11). doi:10.1029/2012JB009540.

Phillips, K., Clayton, R.W., 2014. Structure of the subduction transition region from seismic array data in southern Peru. Geophys. J. Int. 196 (3), 1889–1905. doi:10.1093/gji/ggt504.

Prieto, G.A., Florez, M., Barrett, S.A., Beroza, G.C., Pedraza, P., Blanco, J.F., Poveda, E., 2013. Seismic evidence for thermal runaway during intermediate-depth earthquake rupture. Geophys. Res. Lett. 40, 6064–6068. doi:10.1002/2013GL058109.

Prieto, A.G., Froment, B., Yu, C., Poli, P., Abercrombie, R., 2017. Earthquake rupture below the brittle-ductile transition in continental lithospheric mantle. Sci. Adv. 3, e1602642.

Poli, P., Prieto, G.A., Rivera, E., Ruiz, S., 2016. Earthquakes and thermal shear instability in the Hindu Kush intermediate depth nest. Geophys. Res. Lett. 43 (4), 1537–1542. doi:10.1002/2015GL067529.

Poli, P., Prieto, G.A., 2016. Global rupture parameters for deep and intermediate-depth earthquakes. J. Geophys. Res. 121 (12), 8871–8887. doi:10.1002/2016JB013521.

Poli, P., Prieto, G.A., 2014. Global and along-strike variations of source duration and scaling for intermediate-depth and deep-focus earthquakes. Geophys. Res. Lett. 41 (23), 8315–8324. doi:10.1002/2014GL061916.

Pugh, S.F., 1954. Relations between the elastic moduli and the plastic properties of polycrystalline pure metals. Philos. Mag. 45, 823. doi:10.1080/14786440808520496.

Raterron, P., Girard, J., Chen, J.H., 2012. Activities of olivine slip systems in the upper mantle. Phys. Earth Planet. Inter. 200, 105–112. doi:10.1016/j.pepi.2012.04.006.

Ravindran, P., Fast, L., Korzhavyi, P.A., Johansson, B., 1998. Density functional theory for calculation of elastic properties of orthorhombic crystals: application to TiS_2. J. Appl. Phys. 84, 4891–4904. doi:10.1063/1.368733.

Roberts, D.C. & Turcotte, D.L., 2000. in Geocomplexity and the Physics of Earthquakes (eds Rundle, J. B., Turcotte D. L. & Klein, W.) 97–103, AGU.

Rubie, D.C., Ross, C.R., 1994. Kinetics of the olivine-spinel transformation in subducting lithosphere: experimental constraints and implications for deep slab processes. Phys. Earth Planet. Inter. 86, 223–243. doi:10.1016/0031-9201(94)05070-8.

Ruiz, S., Tavera, H., Poli, P., Herrera, C., Flores, C., Rivera, E., Madariaga, R., 2017. The deep Peru 2015 doublet earthquakes. Earth Planet. Sci. Lett. 478, 102–109. doi:10.1016/j.epsl.2017.08.036.

Samae, V., Cordier, P., Demouchy, S., Bollinger, C., Gasc, J., Koizumi, S., Mussi, A., Schryvers, D., Idrissi, H., 2021. Stress-induced amorphization triggers deformation in the lithospheric mantle. Nature 591, 82–86. doi:10.1038/s41586-021-03238-3.

Schubnel, A., Brunet, F., Hilairet, N., Gasc, J., Wang, Y.B., Green, H.W., 2013. Deep-focus earthquake analogs recorded at high pressure and temperature in the laboratory. Science 341, 1377–1380. doi:10.1126/science.1240206.

Shen, Z.C., Zhan, Z.W., 2020. Metastable olivine wedge beneath the Japan sea imaged by seismic interferometry. Geophys. Res. Lett. 47, 1–8. doi:10.1029/2019GL085665.

Shearer, P.M., 2019. Introduction to Seismology. Cambridge University Press, Cambridge (UK), p. 442. doi:10.1017/9781316877111.

Silver, P.G., Beck, S.L., Wallace, T.C., Meade, C., Myers, S.C., James, D.E., Kuehnel, R., 1995. Rupture characteristics of the deep Bolivian earthquake of 9 June 1994 and the mechanism of deep-focus earthquakes. Science 268, 69. doi:10.1126/science.268.5207.69, -69.

Sin'ko, G.V., Smirnov, N.A., 2002. Ab initio calculations of elastic constants and thermodynamic properties of bcc, fcc, and hcp Al crystals under pressure. J. Phys. Condens. Matter 14, 6989.

Somoza, R., Ghidella, M.E., 2012. Late Cretaceous to recent plate motions in western South America revisited. Earth and Planet. Sci. Lett. 331, 152–163. doi:10.1016/j.epsl.2012.03.003.

Spottiswoode, S.M., McGarr, A., 1975. Source parameters of tremors in a deep-level gold mine. Bull. Seism. Soc. Am. 65, 93–112.

Spudich, P.K.P., 1992. On the inference of absolute stress levels from seismic radiation. Tectonophysics 211, 99–106. doi:10.1016/0040-1951(92)90053-9.

Stein, S., Engeln, J.F., DeMets, C., Gordon, R.G., Woods, D., Lundgren, P., Wiens, D.A., 1986. The Nazca-South America convergence rate and the recurrence of the Great 1960 Chilean Earthquake. Geophys. Res. Lett. 13 (8), 713–716. doi:10.1029/GL013i008p00713.

Sung, C.M., Burns, R.G., 1976. Kinetics of high-pressure phase transformations: implications to the evolution of the olivine- spinel transition in the downgoing lithosphere and its consequences on the dynamics of the mantle. Tectonophysics 31, 1–32.

Tavera, H., Buforn, E., 2001. Source mechanism of earthquakes in Peru. J. Seismol. 5 (4), 519–540.

Terakawa, T., Hauksson, E., 2018. Absolute stress fields in the source region of the 1992 Landers Earthquake. J. Geophys. Res. Solid Earth 123, 8874–8890. doi:10.1029/2018JB015765.

Vallée, M., Charléty, J., Ferreira, A.M., Delouis, B., Vergoz, J., 2011. SCARDEC: a new technique for the rapid determination of seismic moment magnitude, focal mechanism and source time functions for large earthquakes using body-wave deconvolution. Geophys. J. Int. 184 (1), 338–358. doi:10.1111/j.1365-246X.2010.04836.x.

Vallée, M., 2013. Source time function properties indicate a strain drop independent of earthquake depth and magnitude. Nat. Commun. 4, 3606. doi:10.1038/ncomms3606.

Vallée, M., Douet, V., 2016. A new database of source time functions (STFs) extracted from the SCARDEC method. Phys. Earth Planet. Inter. 257, 149–157. doi:10.1016/j.pepi.2016.05.012.

Vassiliou, M.S., Kanamori, H., 1982. The energy release in earthquakes. Bull. Seismol. Soc. Am. 72 (2), 371–387.

Venkataraman, A., Kanamori, H., 2004. Effect of directivity on estimates of radiated seismic energy. J. Geophys. Res.: Solid Earth 109 (B4), B04301. doi:10.1029/2003JB002548.

Vidale, J.E., Houston, H., 1993. The depth dependence of earthquake duration and implications for rupture mechanisms. Nature 365 (6441), 45–47. doi:10.1038/365045a0.

Vitos, L., 2007. Computational Quantum Mechanics For Materials Engineers: the EMTO Method and Applications. Springer-Verlag, London.

Wang, J.H., 2004. The seismic efficiency of the 1999 Chi-Chi, Taiwan, earthquake. Geophys. Res. Lett. 31, L10613. doi:10.1029/2004GL019417.

Wang, Y.B., Zhu, L.P., Shi, F., Schubnel, A., Hilairet, N., Yu, T., Rivers, M., Gasc, J., Addad, A., Deldicque, D., Li, Z.Y., Brunet, F., 2017. A laboratory nanoseismological study on deep-focus earthquake micromechanics. Sci. Adv. 3, 1–12. doi:10.1126/sciadv.1601896.

Wiens, D.A., McGuire, J.J., 1995. The 1994 Bolivia and Tonga events: fundamentally different types of deep earthquakes? Geophys. Res. Lett. 22, 2245–2248. doi:10.1029/95GL01598.

Wiens, D.A., Gilbert, H.J., 1996. Effect of slab temperature on deep-earthquake aftershock productivity and magnitude-frequency relations. Nature 384, 153–156. doi:10.1038/384153a0.

Wiens, D.A., 2001. Seismological constraints on the mechanism of deep earthquakes: temperature dependence of deep earthquake source properties. Phys. Earth Planet. Inter. 127, 145–163. doi:10.1016/S0031-9201(01)00225-4.

Ye, L., Lay, T., Kanamori, H., Koper, K.D., 2013. Energy release of the 2013 Mw 8.3 Sea of Okhotsk earthquake and deep slab stress heterogeneity. Science 341 (6152), 1380–1384. doi:10.1126/science.1242032.

Ye, L., Lay, T., Kanamori, H., Zhan, Z., Duputel, Z., 2016a. Diverse rupture processes in the 2015 Peru deep earthquake doublet. Sci. Adv. 2, e1600581 2016.

Ye, L., Lay, T., Kanamori, H., Rivera, L., 2016b. Rupture characteristics of major and great ($Mw \geq 7.0$) megathrust earthquakes from 1990 to 2015: 1. Source parameter scaling relationships. J. Geophys. Res. Solid Earth 121, 845–863. doi:10.1002/2015JB012427.

Zha, C.S., Duffy, T.S., Downs, R.T., Mao, H.K., Hemley, R.J., 1998. Brillouin scattering and X-ray diffraction of San Carlos olivine: direct pressure determination to 32 GPa. Earth Planet. Sci. Lett. 159, 25–33. doi:10.1016/S0012-821X(98)00063-6.